



NAVAL POSTGRADUATE SCHOOL

MONTEREY, CALIFORNIA

THESIS

**CERAMIC SPHERE FRONT FACE ARMOR SYSTEM
PERFORMANCE ASSESSMENT AGAINST RIFLED
PROJECTILES**

by

Rochelle E. Clark

December 2021

Thesis Advisor:
Second Reader:

Raymond M. Gamache
Keith R. Cohn

Approved for public release. Distribution is unlimited.

THIS PAGE INTENTIONALLY LEFT BLANK

REPORT DOCUMENTATION PAGE			<i>Form Approved OMB No. 0704-0188</i>	
Public reporting burden for this collection of information is estimated to average 1 hour per response, including the time for reviewing instruction, searching existing data sources, gathering and maintaining the data needed, and completing and reviewing the collection of information. Send comments regarding this burden estimate or any other aspect of this collection of information, including suggestions for reducing this burden, to Washington headquarters Services, Directorate for Information Operations and Reports, 1215 Jefferson Davis Highway, Suite 1204, Arlington, VA 22202-4302, and to the Office of Management and Budget, Paperwork Reduction Project (0704-0188) Washington, DC, 20503.				
1. AGENCY USE ONLY (Leave blank)	2. REPORT DATE December 2021	3. REPORT TYPE AND DATES COVERED Master's thesis		
4. TITLE AND SUBTITLE CERAMIC SPHERE FRONT FACE ARMOR SYSTEM PERFORMANCE ASSESSMENT AGAINST RIFLED PROJECTILES			5. FUNDING NUMBERS	
6. AUTHOR(S) Rochelle E. Clark				
7. PERFORMING ORGANIZATION NAME(S) AND ADDRESS(ES) Naval Postgraduate School Monterey, CA 93943-5000			8. PERFORMING ORGANIZATION REPORT NUMBER	
9. SPONSORING / MONITORING AGENCY NAME(S) AND ADDRESS(ES) N/A			10. SPONSORING / MONITORING AGENCY REPORT NUMBER	
11. SUPPLEMENTARY NOTES The views expressed in this thesis are those of the author and do not reflect the official policy or position of the Department of Defense or the U.S. Government.				
12a. DISTRIBUTION / AVAILABILITY STATEMENT Approved for public release. Distribution is unlimited.			12b. DISTRIBUTION CODE A	
13. ABSTRACT (maximum 200 words) <p>Current ceramic body armor consists of a monolithic front plate. These monolithic plates have performance degradation issues from fracture due to both multi-hit damage and mishandling. In addition, the plates provide no flexibility. Ceramic spheres have a demonstrated higher mass efficiency compared to monolithic ceramic plates against spherical projectiles and avoid current issues found within monolithic ceramic plates.</p> <p>Within this thesis, rifled projectiles were used to assess the performance and mass efficiency of single-layer ceramic sphere matrices as a front face armor system. Ceramic sphere armor systems varied by ceramic chemistry, diameter size, and encapsulation. A 25.4 mm smooth bore light gas gun was used in combination with a high-speed video camera to capture the initial and terminal velocity after ballistic impact of a 0.30 caliber M2AP projectile with the front face ceramic armor systems. Both the total work and mass efficiency were calculated and compared between both ceramic spheres and monolithic ceramic plate body armor systems.</p>				
14. SUBJECT TERMS body armor, ceramic spheres, rifle projectiles, penetration resistance			15. NUMBER OF PAGES 91	
			16. PRICE CODE	
17. SECURITY CLASSIFICATION OF REPORT Unclassified	18. SECURITY CLASSIFICATION OF THIS PAGE Unclassified	19. SECURITY CLASSIFICATION OF ABSTRACT Unclassified	20. LIMITATION OF ABSTRACT UU	

THIS PAGE INTENTIONALLY LEFT BLANK

Approved for public release. Distribution is unlimited.

**CERAMIC SPHERE FRONT FACE ARMOR SYSTEM PERFORMANCE
ASSESSMENT AGAINST RIFLED PROJECTILES**

Rochelle E. Clark
Lieutenant, United States Navy
BS, Virginia Military Institute, 2014

Submitted in partial fulfillment of the
requirements for the degree of

MASTER OF SCIENCE IN APPLIED PHYSICS

from the

**NAVAL POSTGRADUATE SCHOOL
December 2021**

Approved by: Raymond M. Gamache
Advisor

Keith R. Cohn
Second Reader

Joseph P. Hooper
Chair, Department of Physics

THIS PAGE INTENTIONALLY LEFT BLANK

ABSTRACT

Current ceramic body armor consists of a monolithic front plate. These monolithic plates have performance degradation issues from fracture due to both multi-hit damage and mishandling. In addition, the plates provide no flexibility. Ceramic spheres have a demonstrated higher mass efficiency compared to monolithic ceramic plates against spherical projectiles and avoid current issues found within monolithic ceramic plates.

Within this thesis, rifled projectiles were used to assess the performance and mass efficiency of single-layer ceramic sphere matrices as a front face armor system. Ceramic sphere armor systems varied by ceramic chemistry, diameter size, and encapsulation. A 25.4 mm smooth bore light gas gun was used in combination with a high-speed video camera to capture the initial and terminal velocity after ballistic impact of a 0.30 caliber M2AP projectile with the front face ceramic armor systems. Both the total work and mass efficiency were calculated and compared between both ceramic spheres and monolithic ceramic plate body armor systems.

THIS PAGE INTENTIONALLY LEFT BLANK

TABLE OF CONTENTS

I.	INTRODUCTION.....	1
II.	BACKGROUND	3
A.	BODY ARMOR STANDARDS	3
B.	AMMUNITION.....	5
C.	MODERN BODY ARMOR SYSTEMS.....	7
	1. Composition.....	7
	2. Design Issues.....	10
D.	CERAMIC CHEMICAL PROPERTIES	12
E.	ENCAPSULATION.....	13
F.	THESIS ORGANIZATION AND RESEARCH QUESTIONS.....	14
III.	EXPERIMENTAL SETUP AND COMPUTATIONAL DATA.....	15
G.	LIGHT GAS GUN TESTING	15
	3. Light Gas Gun Components	15
	4. Video Capturing.....	21
	5. Testing Methodology	24
	6. TEMA Setup.....	24
	7. File Output.....	28
H.	DATA PROCESSING	28
I.	TEST MATRIX.....	31
IV.	DATA	37
J.	POSITION VS. TIME	37
K.	VELOCITY OVER TIME	38
L.	ACCELERATION OVER TIME.....	41
V.	DATA ANALYSIS	43
M.	INSTANTANEOUS WORK VS. TIME	43
N.	KINETIC ENERGY DISSIPATED/WORK SUMMATION OVER TIME	46
O.	INSTANTANEOUS KINETIC ENERGY AND WORK VS. TIME.....	52
P.	KINETIC ENERGY LOSS AND TOTAL WORK	56
Q.	MASS EFFICIENCY.....	62
VI.	CONCLUSION	65

LIST OF REFERENCES	67
INITIAL DISTRIBUTION LIST	71

LIST OF FIGURES

Figure 1.	NIJ Standards for acceptable bullets. Source: [10].	4
Figure 2.	NIJ Performance test requirements. Source: [10].	5
Figure 3.	Kinetic energy density for the core of various ammunitions. Source: [14].	7
Figure 4.	Body armor system composition. Source: [14].	8
Figure 5.	ESAPI strike face. Source: [2].	10
Figure 6.	X-radiographic of a hard armor plate from a M2AP projectile. Source: [14].	11
Figure 7.	Ceramic plate comprised of 3/8" AD90 ceramic spheres.	13
Figure 8.	Light gas gun. Source: [2].	16
Figure 9.	3D printed sabot.	17
Figure 10.	Target holders: 3D printed using sparse polycarbonate. Source: [2].	18
Figure 11.	Target mounting system. Source: [1].	18
Figure 12.	0.635 cm Al ₂ O ₃ AD995 sample target adhered to target holder.	19
Figure 13.	High pressure compressor. Source: [2].	20
Figure 14.	Dry air storage tanks. Source: [2].	20
Figure 15.	Light gas gun breech and pressure control valves. Source: [1].	21
Figure 16.	Shimadzu HPV-2 (high-speed video) camera and two LED lights lined up to the port window of the impact chamber. Source: [2].	22
Figure 17.	Silver lined break screen.	23
Figure 18.	Trigger control box. Source: [2].	23
Figure 19.	TEMA scaling setup.	25
Figure 20.	TEMA point three tracker setup.	26
Figure 21.	TEMA multi and single axis graphs.	28

Figure 22.	TEMA plot of velocity verses time for ¼” AD90 spheres encapsulated in P1000 shot at 5000 psi. Initial velocity ~ 640 m/s. Final velocity ~ 550 m/s.	29
Figure 23.	Sample target of AD90 ¼” ceramic spheres.	32
Figure 24.	Al ₂ O ₃ ceramic spheres of different alumina purities. Left is 99.5% alumina; Right is 90% purity.	33
Figure 25.	0.635 cm and 0.952 cm Al ₂ O ₃ ceramic spheres, both 90% alumina.	33
Figure 26.	0.635 cm and 0.952 cm Al ₂ O ₃ ceramic spheres, both 90% alumina and encapsulated in Versalink P1000.	34
Figure 27.	Position vs. time at breech pressure of 5000 psi for each of the eight sample targets.....	37
Figure 28.	Position vs. time at breech pressure of 4000 psi for each of the eight sample targets.....	38
Figure 29.	Position vs. time at breech pressure of 3000 psi for each of the eight sample targets.....	38
Figure 30.	Velocity vs. time at breech pressure 5000 psi for each of the eight sample targets.....	39
Figure 31.	Velocity vs. time at breech pressure 4000 psi for each of the eight sample targets.....	40
Figure 32.	Velocity vs. time at breech pressure 3000 psi for each of the eight sample targets.....	40
Figure 33.	Acceleration vs. time at breech pressure of 5000 psi for each of the eight sample targets.....	41
Figure 34.	Acceleration vs. time at breech pressure of 4000 psi for each of the eight sample targets.....	42
Figure 35.	Acceleration vs. time at breech pressure of 3000 psi for each of the eight sample targets.....	42
Figure 36.	Instantaneous work vs. time at breech pressure 5000 psi for the eight sample targets.....	44
Figure 37.	Instantaneous work vs. time at breech pressure 5000 psi for AD90.....	45
Figure 38.	Instantaneous work vs. time at breech pressure 5000 psi for AD90 vs. AD995 spheres.	46

Figure 39.	Kinetic energy dissipation and work summation vs. time at breech pressure 5000 psi for SiC tile.....	47
Figure 40.	Kinetic energy dissipation and work summation vs. time at breech pressure 5000 psi for AD90 tile.	47
Figure 41.	Kinetic energy dissipation and work summation vs. time at breech pressure 5000 psi for 0.635 cm AD90 spheres no encapsulation.	48
Figure 42.	Kinetic energy dissipation and work summation vs. time at breech pressure 5000 psi for 0.635 cm AD995 spheres no encapsulation.	48
Figure 43.	Kinetic energy dissipation and work summation vs. time at breech pressure 5000 psi for 0.952 cm AD90 spheres no encapsulation.	49
Figure 44.	Kinetic energy dissipation and work summation vs. time at breech pressure 5000 psi for 0.952 cm AD995 spheres no encapsulation.	49
Figure 45.	Kinetic energy dissipation and work summation vs. time at breech pressure 5000 psi for 0.635 cm AD90 spheres encapsulated in P1000.	50
Figure 46.	Kinetic energy dissipation and work summation vs. time at breech pressure 5000 psi for 0.952 cm AD90 spheres encapsulated in P1000.	50
Figure 47.	Kinetic energy dissipation vs. time at breech pressure 5000 psi for all eight sample targets.....	51
Figure 48.	Work summation vs. time at breech pressure 5000 psi for all eight sample targets.....	51
Figure 49.	Instantaneous kinetic energy and work vs. time for SiC tile at 5000 psi.....	52
Figure 50.	Instantaneous kinetic energy and work vs. time for AD90 tile at 5000 psi.....	53
Figure 51.	Instantaneous kinetic energy and work vs. time for 0.635 cm AD90 spheres no encapsulation at 5000 psi.....	53
Figure 52.	Instantaneous kinetic energy and work vs. time for 0.635 cm AD995 spheres no encapsulation at 5000 psi.....	54
Figure 53.	Instantaneous kinetic energy and work vs. time for 0.952 cm AD90 spheres no encapsulation at 5000 psi.....	54

Figure 54.	Instantaneous kinetic energy and work vs. time for 0.635 cm AD995 spheres no encapsulation at 5000 psi.	55
Figure 55.	Instantaneous kinetic energy and work vs. time for 0.635 cm AD90 spheres encapsulated in P1000 at 5000 psi.	55
Figure 56.	Instantaneous kinetic energy and work vs. time for 0.952 cm AD90 spheres encapsulated in P1000 at 5000 psi.	56
Figure 57.	Kinetic energy loss vs. velocity for SiC tile.	57
Figure 58.	Kinetic energy loss vs. velocity for AD90 tile.....	57
Figure 59.	Kinetic energy loss vs. velocity for 0.635 cm AD90 spheres no encapsulation.....	58
Figure 60.	Kinetic energy loss vs. velocity for 0.635 cm AD995 spheres no encapsulation.....	58
Figure 61.	Kinetic energy loss vs. velocity for 0.952 cm AD90 spheres no encapsulation.....	59
Figure 62.	Kinetic energy loss vs. velocity for 0.952 cm AD995 spheres no encapsulation.....	59
Figure 63.	Kinetic energy loss vs. velocity for 0.635 cm AD90 spheres encapsulated in P1000.....	60
Figure 64.	Kinetic energy loss vs. velocity for 0.952 cm AD90 spheres encapsulated in P1000.....	60
Figure 65.	Kinetic energy loss for all eight sample targets at breech pressure 5000 psi.	61
Figure 66.	Mass efficiency for all eight sample targets.	63

LIST OF TABLES

Table 1.	Table of select small arms projectiles. Source: [14]	6
Table 2.	Key properties of high-performance materials. Source: [16].	9
Table 3.	Properties of common strike face materials. Source: [14].	9
Table 4.	Mechanical properties of ceramics. Adapted from [21]–[24].	12
Table 5.	Hugoniot variables.	27
Table 6.	Hugoniot results from Labview program.	27
Table 7.	Density of materials. Sources: [21], [23], [24].	31
Table 8.	Test matrix of shots performed in this study.	35
Table 9.	Calculated kinetic energy loss for all eight sample targets at breech pressure 5000 psi.	62
Table 10.	Calculated mass efficiency for all eight sample targets.	63

THIS PAGE INTENTIONALLY LEFT BLANK

LIST OF ACRONYMS AND ABBREVIATIONS

2D	two-dimensional space
3D	three-dimensional space
DAP	Deltoid and Auxiliary Protector
DARPA	Defense Advanced Research Projects Agency
DTG	date time group
DOD	Department of Defense
DOT&E	Director, Operational Test and Evaluation
ESAPI	enhanced small arms protective insert
ESBI	enhanced side ballistic insert
ft/s	feet per second
HAP	hard armor plate
IBA	INTERCEPTOR Multi-Threat Body Armor System
IOTV	improved outer tactical vest
J	Joules
LED	light-emitting diode
M2AP	armor piercing 0.30 caliber bullet
Mfps	million frames per second
m/s	meters per second
NATO	North Atlantic Treaty Organization
ns	nanosecond
NIJ	National Institute of Justice
NPS	Naval Postgraduate School
psi	pound-force per square inch
SAPI	Small Arms Protective Insert
SI	Système international d'unités
TEMA	TrackEye Motion Analysis
UHMWPE	ultra-high molecular weight polyethylene
U.S.	United States
USSOCOM	United States Special Operations Command
V	volts

THIS PAGE INTENTIONALLY LEFT BLANK

ACKNOWLEDGMENTS

I would like to take the time to thank my thesis advisor, Dr. Raymond Gamache, for his patience, knowledge, hard work, and ingenuity while we worked together to understand the ceramics to another level. His expertise furthered my knowledge and capacity to research this topic from initial understandings to analysis of my data. I would also like to thank Dr. Joseph Hooper for his expertise of shock physics that assisted my basic understanding of ballistic impacts via his classes on terminal ballistics and explosives. I would like to thank Dr. Keith Cohn as my second reader and his knowledge while assisting me in furthering my MATLAB programming skills. Additionally, I would like to thank Robin Nicolai for his technical assistance using the TEMA software.

Finally, I would like to thank my husband, Sean, for his understanding and support of me and our family which allowed me to focus my time and effort into completing this research.

THIS PAGE INTENTIONALLY LEFT BLANK

I. INTRODUCTION

The body armor system in current use by the Department of Defense (DOD) comprises of a monolithic ceramic front plate backed by ultra-high molecular weight polyethylene (UHMWPE) textile armor backing system. The front plate is designed to stop higher velocity rifled threats but has some significant downfalls. The monolithic plate is not flexible, has high maintenance costs requiring specific storage requirements due to susceptibility to cracking and higher areal density compared to textile armor systems, and has considerably degraded performance from multiple impacts. The application of ceramic spheres as a front face armor system supports a lighter, flexible armor that additionally, enables multi-hit performance, and reduced damage from mishandling.

This thesis investigates the performance of this new front plate system consisting of ceramic spheres against the 0.30 caliber M2AP projectile. High-speed video imaging (5 Mfps) combined with video tracking software TrackEye Motion Analysis (TEMA) can enable position variation with a time resolution of 200 ns. Through measurement of positional changes as a function of time, this capability enables the determination of velocity and acceleration during impact. Through these measured dynamic values, both the kinetic energy loss as well as the work performed to resist penetration can be estimated; this enables the determination of the penetration resistance performance as well as the mass efficiency of each target system.

Targets studied within this thesis consist of both ceramic sphere systems of varied diameters, chemistries, and encapsulations as well as ceramic tile systems used as a control. Previous theses have evaluated similar target systems against chromium steel sphere projectiles [1], [2].

The energy loss for a 0.30 caliber M2AP bullet impacting each sample target at three separate impact velocities was studied both as a function of kinetic energy loss and work performed by the target. Each type of target will be studied for energy loss, total work, and mass efficiency. These measurements will be analyzed and compared between the performance of ceramic spheres and monolithic ceramic plates. From this analysis, the

penetration resistance performance of front face ceramic sphere systems against the 0.30 caliber M2AP will be quantified.

II. BACKGROUND

Body armor has been used and improved upon for centuries. In the 1960s and 1970s, Wilkins conducted multiple studies on ceramic light armor which has become the foundation to many modern body armor systems [3]–[6]. Currently, the DOD uses a monolithic silicon carbide and boron carbide as the ceramics for front armor plate systems with an UHMWPE backing. This type of body armor system will be referred to as a Small Arms Protective Insert (SAPI) or the increased performance version Enhanced Small Arms Protective Insert (ESAPI) plates [7]. While the SAPI and ESAPI plates are capable of stopping 7.62 mm rifled rounds, they have some significant issues [7]. The SAPI was designed for National Institute of Justice (NIJ) level III threats (M80), and the ESAPI plates were designed to defeat NIJ level IV threats (0.30 caliber M2AP) [8]. Both plate systems enable performance to defeat the first round, but multi-hit capacity is affected by fracture propagation [9]. SAPI and ESAPI systems are also susceptible to damage (and diminished performance) due to mishandling [8].

This thesis will concentrate on a new approach to front face armor systems where single piece monolithic ceramic plates are replaced with ceramic sphere systems. The proposed design will be investigated based upon its penetration performance. If the ceramic sphere performance can meet either SAPI or ESAPI performance, intrinsic performance capabilities including multi-hit and fracture resistance performance will be enabled.

A. BODY ARMOR STANDARDS

Body armor standards are defined by the Standards and Testing Program within the NIJ as part of the Homeland Security Act of 2002 [10]. This program is directed to establish and maintain the performance standards for federal, state and local authorities within the United States [10]. NIJ has divided personal body armor into five levels of classification, as listed in Figure 1, as part of NIJ 0101.06 [10]. The NIJ has been working to update the guidelines that will redefine test standards, determine differences between male and female wearers, and reorganize the threat levels [11]. The new standards will be called NIJ 0101.07 but are still in draft as of November 2021.

Threat Level	Caliber	Bullet Weight	BULLET DESCRIPTION	Nominal Bullet Diameter	Acceptable Manufacturer	Bullet Model Number
IIA	9 mm Luger	8.0 g (124 gr)	FMJ RN	9 mm (.355 in)	Remington	23558
	.40 S&W	11.7 g (180 gr)	FMJ	10 mm (.400 in)	Remington	23686
II	9 mm Luger	8.0 g (124 gr)	FMJ RN	9 mm (.355 in)	Remington	23558
	.357 Mag	10.2 g (158 gr)	JSP	9.1 mm (.357 in)	Remington	22847
IIIA	.357 SIG	8.1 g (125 gr)	TMJ	9.0 mm (.355 in)	Speer	4362
	.44 Mag	15.6 g (240 gr)	JHP	10.9 mm (.429 in)	Speer	4453 or 4736**
III	7.62 mm NATO	9.6 g (147 gr)	FMJ – SPIRE PT BT*	7.62 mm (.308 in)	***	***
IV	30.06 M2 AP	10.8 g (166 gr)	FMJ – SPIRE PT AP	7.62 mm (.308 in)	May be obtained from U.S. Military M2 AP ammunition	

* Verify that jacket is ferrous (use of a magnet is acceptable).

** Note: These two models are the same bullet but sold in different quantities.

*** Bullet may be obtained from U.S. military/NATO M80 ammunition, or from other manufacturers meeting the specifications for the projectile in the M80 cartridge.

Figure 1. NIJ Standards for acceptable bullets. Source: [10].

This thesis will specifically be comparing data results to NIJ threat levels IV. Threat level IV is specified for hard armor plates (HAP) or inserts against the 0.30 caliber armor piercing bullets (M2AP) [10].

The specifications for testing new armor to meet these threat levels is listed in Figure 2. NIJ threat level III is required to withstand six shots per panel of 7.62 mm NATO FMJ at 847 m/s (2780 ft/s) test velocity. The NIJ threat level IV is required to withstand one to six shots per panel of .30 Caliber M2AP at 878 m/s (2880 ft/s). Under the NIJ 0101.07 standards, the threat level nomenclature will change to be more specific [11]. Level III and IV will soon be updated to RF1 and RF3, respectively, representing the rifle threats [11]. There will also be an additional threat level RF2 as an intermediate threat level [11].

TEST VARIABLES						PERFORMANCE REQUIREMENTS			SHOT REQUIREMENTS					
Armor Type	Test Round	Test Bullet	Bullet Mass	Conditioned Armor Test Velocity*	New Armor Test Velocity*	Hits Per Panel at 0° Angle	Maximum BFS Depth	Hits Per Panel at 30° or 45° Angle [†]	Shots Per Panel	Panel Size	Panel Condition	Panels Required	Shots Required	Total Shots Required
IIA	1	9 mm FMJ RN	8.0 g (124 gr)	355 m/s (1165 ft/s)	373 m/s (1225 ft/s)	4	44 mm (1.73 in)	2	6	Large	New Conditioned	4	24	144
										Small	New Conditioned	2	12	
	2	.40 S&W FMJ	11.7 g (180 gr)	325 m/s (1065 ft/s)	352 m/s (1155 ft/s)	4	44 mm (1.73 in)	2	6	Large	New Conditioned	4	24	
										Small	New Conditioned	2	12	
II	1	9 mm FMJ RN	8.0 g (124 gr)	379 m/s (1245 ft/s)	398 m/s (1305 ft/s)	4	44 mm (1.73 in)	2	6	Large	New Conditioned	4	24	144
										Small	New Conditioned	2	12	
	2	.357 Magnum JSP	10.2 g (158 gr)	408 m/s (1340 ft/s)	436 m/s (1430 ft/s)	4	44 mm (1.73 in)	2	6	Large	New Conditioned	4	24	
										Small	New Conditioned	2	12	
IIA	1	.357 SIG FMJ RN	8.1 g (125 gr)	430 m/s (1410 ft/s)	448 m/s (1470 ft/s)	4	44 mm (1.73 in)	2	6	Large	New Conditioned	4	24	144
										Small	New Conditioned	2	12	
	2	.44 Magnum SJHP	15.6 g (240 gr)	408 m/s (1340 ft/s)	436 m/s (1430 ft/s)	4	44 mm (1.73 in)	2	6	Large	New Conditioned	4	24	
										Small	New Conditioned	2	12	
III	1	7.62 mm NATO FMJ	9.6 g (147 gr)	847 m/s (2780 ft/s)	-	6	44 mm (1.73 in)	0	6	All	Conditioned	4	24	24
IV	1	.30 Caliber M2 AP	10.8 g (166 gr)	878 m/s (2880 ft/s)	-	1 to 6	44 mm (1.73 in)	0	1 to 6	All	Conditioned	4 to 24	24	24
Special	-	Each test threat to be specified by armor manufacturer or procuring organization.				Armor performance and shot requirements shall depend on armor type.								

*Target measurement velocity. Fair hit measurement velocities must be within ± 9.1 m/s (± 30 ft/s) of this value, as defined in Section 7.6.

[†]Each armor that is to be shot at angles other than 0° shall be shot once at a 30° angle and once at a 45° angle.






Figure 2. NIJ Performance test requirements. Source: [10].

In 2009, the DOD Inspector General reviewed standards for ballistic testing and armor plates/inserts [12]. It was determined that there a lack of standardization within the DOD, specifically among Army and United States Special Operations Command (USSOCOM) criteria [12]. The Director, Operational Test and Evaluation (DOT&E) was recommended to work with Army and USSOCOM to develop standard test criteria for body armor, and in 2010, the DOT&E distributed the body armor testing standards [12] [13]. Threat munitions were not specified in the DOT&E standards, so for the purposes of this thesis, NIJ threat levels will be used [13].

B. AMMUNITION

As noted in the previous section, this thesis will focus on the 0.30 caliber M2AP projectile. This projectile is composed of an outer copper cladding encapsulating a hardened steel core. The projectile weight is ~10.7 grams, and has a hardness of 785 Hv [14]. Table 1 is a table of small arms projectiles including the 0.30 caliber M2AP.

Table 1. Table of select small arms projectiles. Source: [14]

Ammunition	9mm FMJ remington	7.62mm M80 NATO bass	7.62×39mm AK47	US 30-06" [AP M2]	7.62mm×51 [FFV]
Bullet and core					
Bullet weight/g	8.0	9.5	7.9	10.7	8.4
Core weight/g	~7.0	~7.0	3.6	5.2	5.9
Core dia/mm	8.0	~7.1	5.7	6.2	5.6
Core material	Lead-based	Lead-based	Mild steel	Hardened steel	Tungsten carbide
Hardness (Hv)	~30	~30	210	785	1 450

When considering ammunition penetration capability, the hardness of the core and shape of the nose (ogive, conical, or blunt) need to be considered [14]. Crouch [14] calculates kinetic energy density for a few different projectiles, as displayed in Figure 3, by dividing the kinetic energy of the projectile's inner core by the surface area of the projectile that impacts the target while using the respective muzzle velocities. As seen in the figure, the kinetic energy density is significantly higher for the M2AP at about $3.3 \text{ J} * \text{mm}^{-2}$ compared to the NIJ level III threat M80 at about $1.7 \text{ J} * \text{mm}^{-2}$ [14].

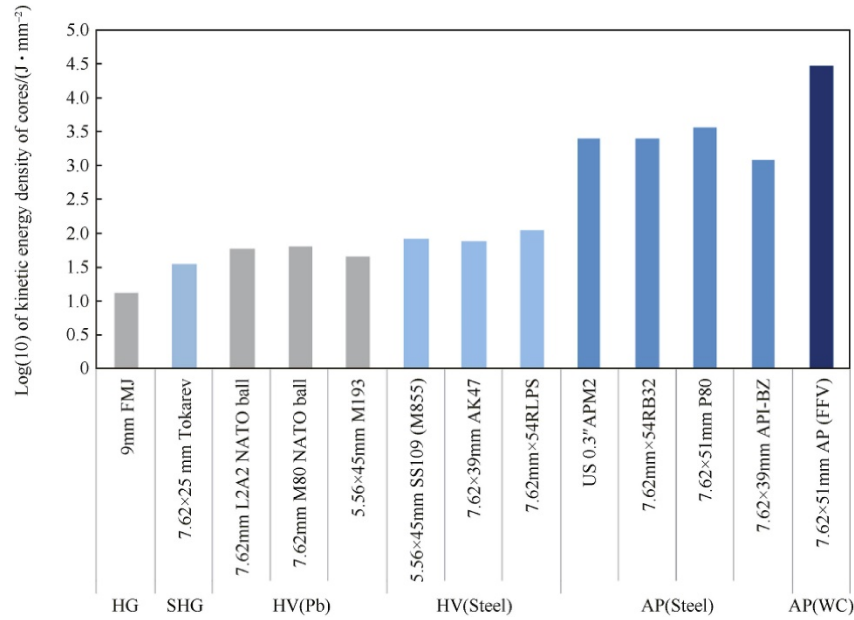


Figure 3. Kinetic energy density for the core of various ammunitions.
Source: [14].

C. MODERN BODY ARMOR SYSTEMS

The INTERCEPTOR Multi-Threat Body Armor System (IBA) consists of an outer tactical vest and small arms-protective protective inserts [7]. This design went into production in 1998 and was fielded in 2002 [7]. The outer tactical vest can stop 9mm bullets but not rifled or machine-gun fire, so inserts are needed to protect against those threats [7]. In the 1990s, Defense Advanced Research Projects Agency (DARPA) created boron carbide (B_4C) body armor inserts that are used in some of the INTERCEPTOR systems while others used silicon carbide (SiC) [7]. The SAPI and ESAPI inserts are capable of stopping rifled projectiles at different performance levels [7].

1. Composition

The IBA is composed of a pair of SAPI/ESAI (front and back), weighing 8.0/10.9 pounds per pair, respectively—the outer tactical vest that weighs 7.7 pounds, a Deltoid and Auxiliary Protector (DAP) weighing 5.3 pounds, and a pair of Enhanced Side Ballistic Inserts (ESBI) weighing 7.1 pounds per set for a total of 28.1/30 pounds for size medium, although weight may change depending on configuration [15]. The IBA plate holder

system incorporates a Kevlar textile armor system forming a continuous protection around the torso against 9 mm rounds [7]. Both the vest and inserts come in sizes extra-small, small, medium, large, and extra-large [7].

SAPI and ESAPI armor plates are inserted into the tactical vest to give the overall system extra protection within the region of vital organs. As previously mentioned, ESAPI armor plates are designed with an increased protection compared to the SAPI inserts. Both armor inserts are comprised of a monolithic ceramic plate called a strike face backed by a textile armor system; the most common textile is UHMWPE [14]. The purpose of the strike face is to slow down, blunt, and erode or shatter the projectile. The front face ceramic system reduces the penetration potential of the projectile enabling the backing material to absorb and arrest the projectile [14]. Figure 4 lays out a body armor system composition with typical materials used for each sub-system.

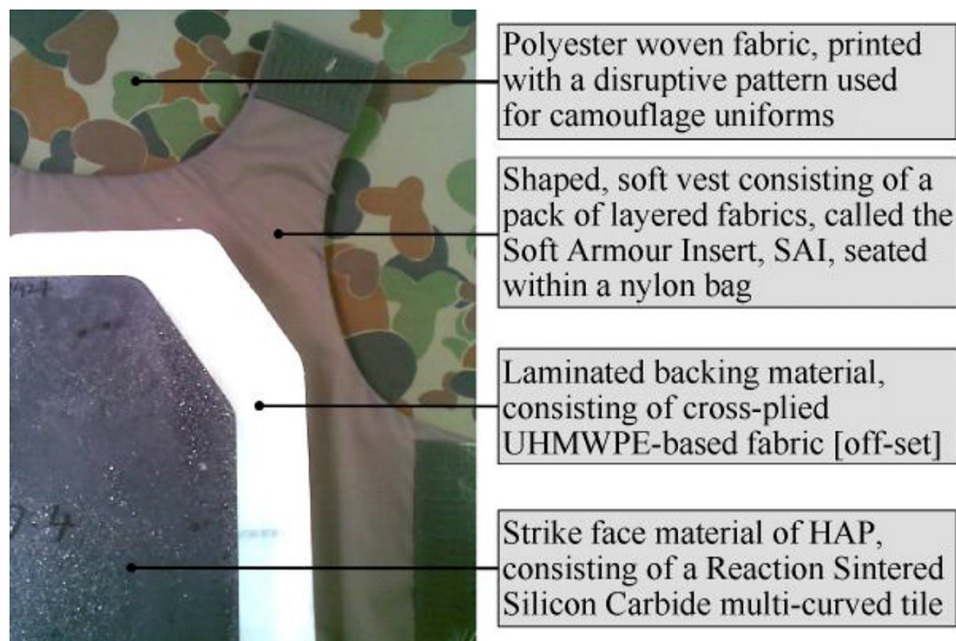


Figure 4. Body armor system composition. Source: [14].

The backing material is typically made from UHMWPE fibers. When the fibers are pressed and laminated, it can stop mild-steel-core 7.62 mm rounds at point blank range [14]. There are many other textile backing materials, but UHMWPE has remained superior

for one reason or another. Zylon AS and HM are two materials that rival UHMWPE by being stronger, but its hygroscopic properties degrade the performance of the Zylon. Table 2 displays the properties of various backing textiles with HS-PE being UHMWPE.

Table 2. Key properties of high-performance materials. Source: [16].

	Tenacity		Modulus		Elonga- tion	Density	Moisture Regain	LOI	Heat Resistance*
	cN/dtex	GPa	cN/dtex	GPa	%	g/cm ³	%		C
Zylon® AS	37	5.8	1150	180	3.5	1.54	2.0	68	650
Zylon® HM	37	5.8	1720	270	2.5	1.56	0.6	68	650
p-Aramid(HM)	19	2.8	850	109	2.4	1.45	4.5	29	550
m-Aramid	4.5	0.65	140	17	22	1.38	4.5	29	400
Steel Fiber	3.5	2.8	290	200	1.4	7.8	0		
HS-PE	35	3.5	1300	110	3.5	0.97	0	16.5	150
PBI	2.7	0.4	45	5.6	30	1.4	15	41	550
Polyester	8	1.1	125	15	25	1.38	0.4	17	260

The strike face is typically composed of a SiC or B₄C monolithic plate. These are typically hot sintered (SiC) or hot pressed (B₄C) to 0.270 ± 0.02 inches with 35–45 layers of UHMWPE [2] [17]. ESAPI inserts are 0.1 inches thicker and incorporates the same backing system [2]. Table 3 is a table of common strike face material properties.

Table 3. Properties of common strike face materials. Source: [14].

Class of material	Source, grade, (reference)	Density/(kg·m ⁻³)	Hardness/GPa	Elastic modulus/GPa	Flexural strength/MPa	Fracture toughness/(MPa·m ^{-1/2})
UHH Steel	SSAB, Armox Advance ^a	7780	2.3	208	NK	15–20
Glass Ceramics	Silceram ^b	2900	7.0	122	180	NK
Alumina	CoorsTek, AD85, ^c	3420	9.4	221	296	3–4
Alumina	CoorsTek, AD998, ^c	3920	14.1	370	375	4–5
AlON	Surmet, ^d	3695	18.5	323	380	~2
TiB ₂	CoorsTek, PAD ^e	4480	26.4	555	275	~7
SiC	CoorsTek, SiC–N, PAD ^e	3200	23.5	460	570	~5
SiC	MCC, RSSC, ^e	3106	24.5	399	504	NK
B ₄ C	CoorsTek, PAD ^e	2500	25.5	460	410	4

2. Design Issues

One major issue with the SAPI and ESAPI is the fragile nature of the ceramic that can easily cause fracturing. Figure 5 is an image of an ESAPI strike face that is clearly marked “Handle with Care” to prevent damage from mishandling. There are specific storage and shipping requirements to prevent the fracturing of the armor plates. SAPI/ESAPI plates within the handling process must avoid being stored more than ten high, and all stacked plated must be of the same size, with strike face downward for proper storage [8]. Additionally, strike faces must be shipped in corrugated boxes with the plates stored vertically and have foam between each plate [8]. From April to June of 2009, approximately seven million dollars’ worth of IBA components were lost due to the U.S. Army’s improper storage, shipping, and maintenance [8].



Figure 5. ESAPI strike face. Source: [2].

D’Aries, a chief scientist for Non-Destructive Evaluation, was quoted in [18], explaining that since the SAPI plates are ceramic, they are brittle and prone to cracking as

ceramic is a glass material. The ceramic front plate absorbs the kinetic energy of the impacting round by shattering to disperse the impact over a large area of the plate [18]. The intended design of the ceramic plate is very effective for one shot, but after one shot, the performance is significantly degraded. This is a major concern from a multiple ballistic impact perspective. Figure 6 displays an X-ray image of a HAP shot with the 0.30 caliber M2AP round. The figure shows radial cracks extending from the impact location to the edge of the plate [14]. This clearly displays the degraded performance of the entire plate from one ballistic impact.

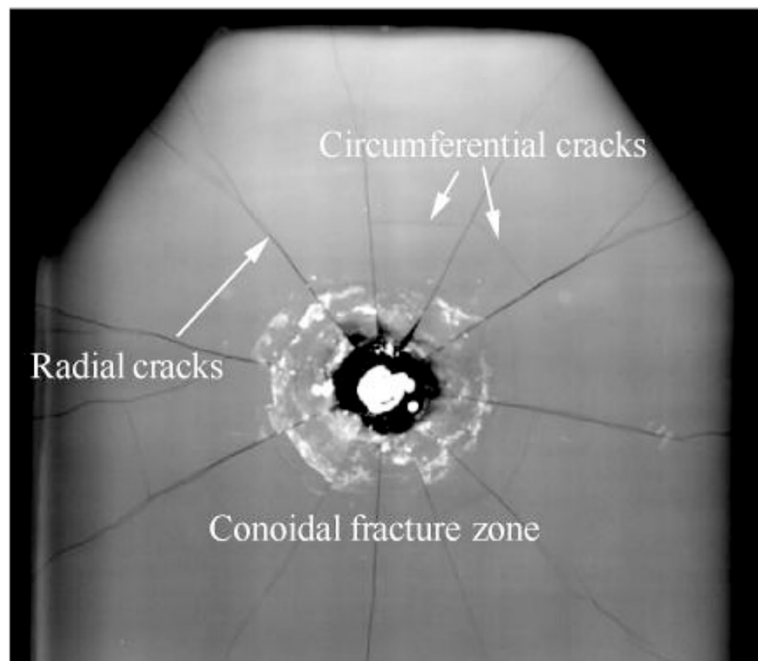


Figure 6. X-radiographic of a hard armor plate from a M2AP projectile.
Source: [14].

Due to the fracturing nature of the ceramic, the plates need to be tested for its ballistic integrity. The SAPI and ESAPI inserts are X-rayed to determine if the plate has any deficiencies [18]. The SAPI and ESAPI inserts can be issued only if they have been scanned within nine months [19]. Since the DOD uses millions of SAPI and ESAPI inserts, this is a significantly expensive maintenance cost. Additionally, this becomes a logistical problem for X-ray sites, mobile X-ray teams, and shipping.

D. CERAMIC CHEMICAL PROPERTIES

Three common ceramics for body armor is aluminum oxide (Al_2O_3), B_4C , and SiC [20]. Table 4 lists key properties for each of these ceramics. Comparing density and compressive strength for the three ceramics, B_4C would be the natural choice for most body armor, but manufacturing costs are high due to the manufacturing process, which requires hot pressing [20]. SiC and Al_2O_3 only require $2,200^\circ\text{C}$ and do not require hot pressing which results in a lower manufacturing cost.

Table 4. Mechanical properties of ceramics. Adapted from [21]–[24].

Ceramics				
	Alumina AD90 (Al_2O_3)	Alumina AD995 (Al_2O_3)	Silicon Carbide (SiC)	Boron Carbide (B_4C)
Density [g/cc]	3.60	3.90	3.07 - 3.14	2.5 - 2.65
Hardness Knoop [kg/mm ²]	10.4	14.1	2800	2550
Elastic Modulus [GPa]	276	370	400	379
Flexural Strength [MPa]	338	379	240	250
Compressive Strength [MPa]	2482	2600	2700	1721
Fracture Toughness [MPa-m ^(1/2)]	3 - 4	4 - 5	4.3	3 - 4
Tensile Strength [MPa]	221	262	307	No value

E. ENCAPSULATION

The proposed design to replace monolithic ceramic plates uses a system of ceramic spheres within a single layer close pack configuration, as seen in Figure 7. Two proven encapsulation technologies include a thin high tensile strength/elongation coating of 6–10 mils or a full encapsulation of a high tensile strength polymers/metals. The key aspect of full encapsulation is the ability to force the fractured ceramic material to remain in the line of flight of the incident projectile. Though the material will not perform as well as the original non-fractured ceramic material, it will enable some resistance and improve the penetration resistance performance.

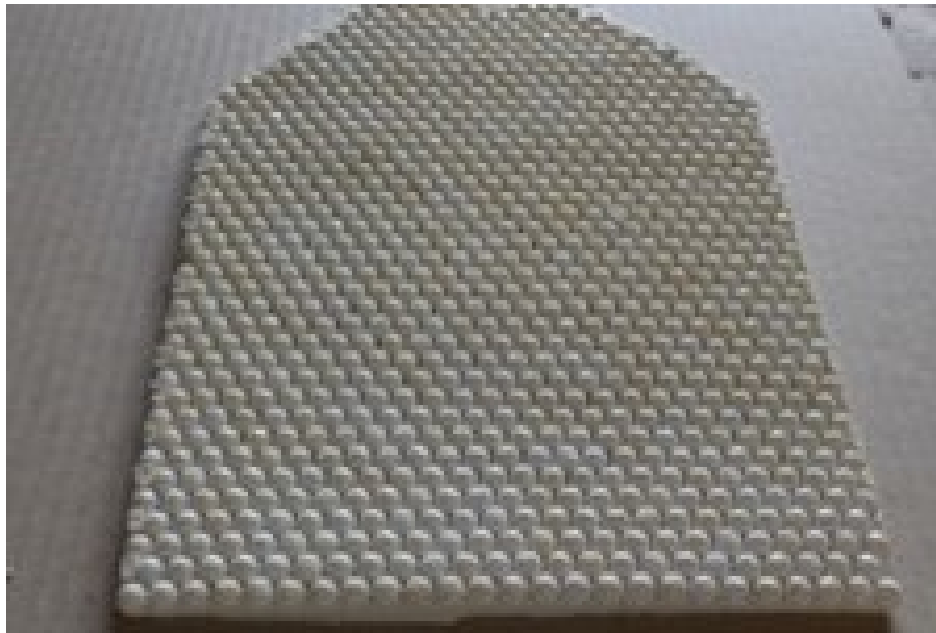


Figure 7. Ceramic plate comprised of 3/8" AD90 ceramic spheres.

This thesis studies a thin ultra-flex coating that holds the spheres with no additional properties and fully encapsulated within Versalink P-1000. The thin ultra-flex coating is water based and has a 2000 psi tensile strength and 2000% elongation. Versalink P-1000 is a polyurea system with an ~ 4 -1 ratio of amine to isocyanate [25]. It has excellent tear resistance, abrasion resistance, heat aging, has high-temperature resistance, long pot life, and is non-hazardous diamine [25]. The Versalink P-1000 has a hardness of 50 (Shore D),

tensile strength of 4500 psi, and elongation of 460% [25]. This material was chosen for its viscoelastic properties, including high modulus and toughness.

F. THESIS ORGANIZATION AND RESEARCH QUESTIONS

This thesis attempts to further research on ceramic sphere armor plates by characterizing work performed on various ceramic sphere chemistries, geometries, and encapsulations against the 0.30 caliber M2AP projectile. Analysis will determine the change in position, velocity, and acceleration as a function of time during impact to determine kinetic energy loss and work performed during ballistic impact at three separate velocities. The calculations can then be used to measure mass efficiency for each sample target to determine the best combination of ceramic sphere systems.

This thesis is divided into six chapters starting with the introduction. The introduction gives a general overview of current ceramic armor plates, issues with the current armor plates, what this research intends to accomplish, and previous studies of ceramic spheres. Chapter II describes the background of ceramic armor starting with body armor standards. This is followed by current threats and ammunition types that this research is designed to protect against.

Chapter III explains the experimental setup, including the test equipment, projectiles, target systems, video capturing, and testing methodology. Then a list of shots and samples are portrayed with explanations of the samples. It also explains the software used to process the video data and how it determines kinematic values. It goes on to explain how the data is evaluated to determine our intended measurements of work performed.

Chapter IV displays and describes the research using experimental and numerical data. The data presented are individual to the sample type and a comparison of the different types.

Chapter V expounds on the data by providing analysis and insight among the samples while amplifying key measurements. Chapter VI concludes this thesis with results and follow-on research work.

Note on units: All units, data, and plots will be in SI units for uniformity.

III. EXPERIMENTAL SETUP AND COMPUTATIONAL DATA

Ballistic testing for this thesis was conducted at Spanagel Hall within Naval Postgraduate School (NPS). The gun system used was a 25.4 mm smooth bore light gas gun with an array of support equipment. Each test was recorded using a high-speed video camera capable of frame rates up to 10 Mfps. The videos were then processed within a motion tracking software (TEMA) enabling tracking of positional changes within video footage providing kinematic data of ballistic trajectories during the exterior and terminal flight of the incident projectile. The data was then analyzed to determine both the kinetic energy loss by the projectile and work performed by the studied target systems during impact. Based on the energy lost and the areal density of the front face system, the mass efficiency of different front face armor systems will be determined.

G. LIGHT GAS GUN TESTING

As noted previously, the gun system used was a 25.4 mm smooth bore light gas gun with a 3.96 m barrel length. This system is comprised of many components that will be discussed in detail. The light gas gun is used for its ability to produce consistent velocities, lower operating costs, and enables fewer safety constraints.

3. Light Gas Gun Components

The light gas gun can operate with compressed gases (dry air, nitrogen, and helium) up to 6000 psi enabling impact velocities of up to 1200 m/s (higher velocities require helium). For all ballistic tests, the light gas gun used helium for the valve control and dry air for the projectile acceleration. The main components of the light gas gun system include breech, smoothbore barrel, impact chamber/catch tank, and control system. Figure 8 displays the light gas gun used which presents: breech, barrel, and catch tank.



Figure 8. Light gas gun. Source: [2].

Firing of the light gas gun incorporates a regenerative breech allowing for a fast release of the pressurized gas. The breech chamber incorporates a piston and plunger. Compressed air is loaded into the breech and held by the plunger behind the projectile until ready to fire.

The breech is mounted to a 2D sliding table enabling separation for projectile loading and reconnection to the barrel system. This style barrel requires the projectile to be contained within a sabot to be fired. Sabots were 3D printed at NPS using a solid polycarbonate filament to form solid serrated petals. The sabots were built of four petals that together had an outside diameter of 2.64 cm that was then machined down to fit precisely within the light gas gun bore. Figure 9 shows two pictures of the 3D printed sabot. The left image is the 0.30 caliber M2AP within the sabot and right is a picture looking into an empty sabot to see the four petals.

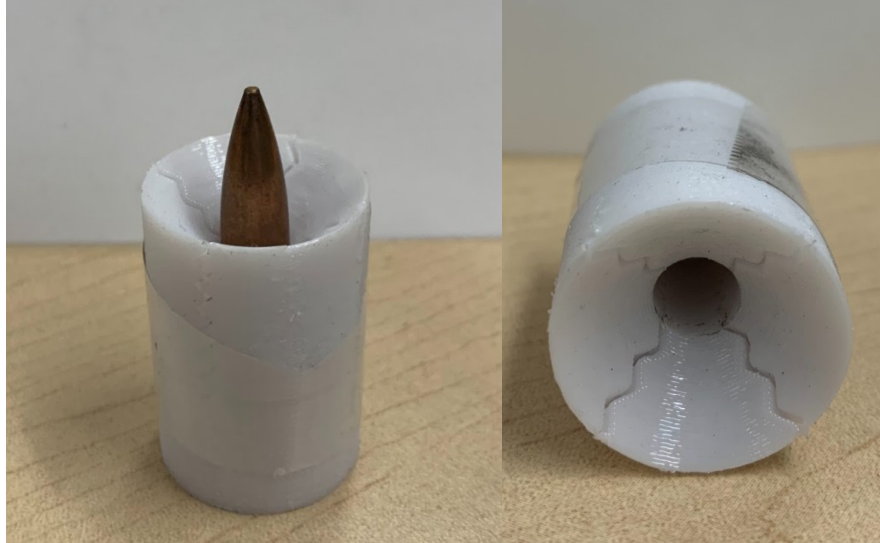


Figure 9. 3D printed sabot.

Beyond the muzzle, of the barrel, is the impact chamber and catch tank. The impact chamber consists of two sections. The first section enables a region of free flight for the sabot/projectile. This region allows for initial aero separation of the sabot from the projectile. A stripper plate placed $\sim 1\text{m}$ from the muzzle enables flight termination of the sabot within the mid tank of the gun system. Beyond the stripper place, within the mid-section, mounting holes are located to mount the targets and align them with the port windows to view impact events.

The target mounting plate consists of a large circular plate with a central cutout and mounting holes to place target samples. The target samples were adhered to a 3D printed target holder. The target holders were also 3D printed at NPS using sparse printed polycarbonate. Two types of holders were used based on the sample type (tile or spheres) as seen in Figure 10. The right design in Figure 10 is designed for heavier samples (such as tiles). Figure 11 displays how the target holder is mounted to the mounting plate. Figure 12 is an example of a target adhered to a target holder.

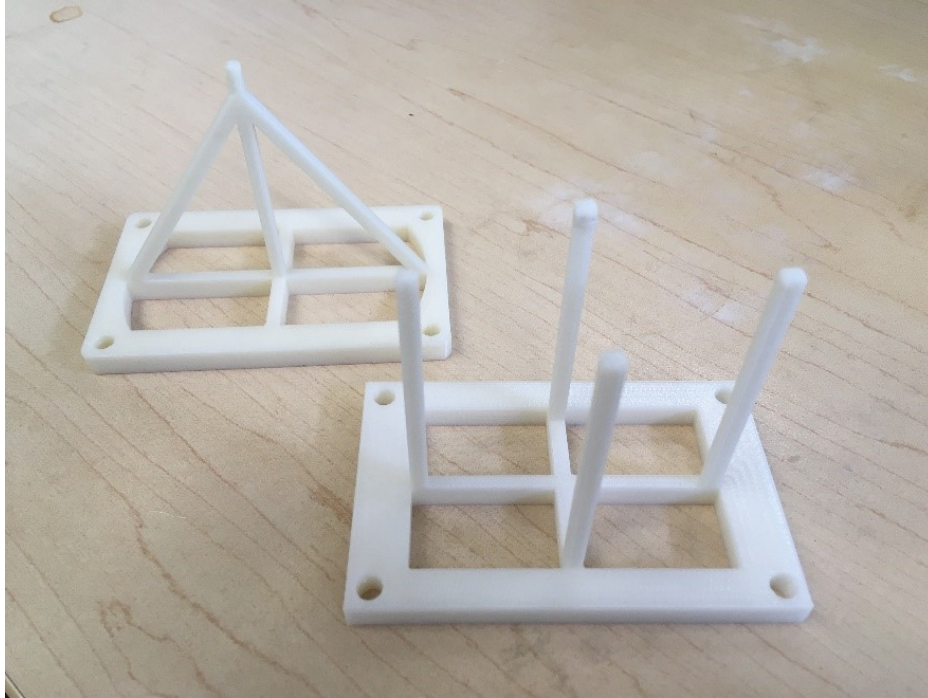


Figure 10. Target holders: 3D printed using sparse polycarbonate. Source: [2].



Figure 11. Target mounting system. Source: [1].

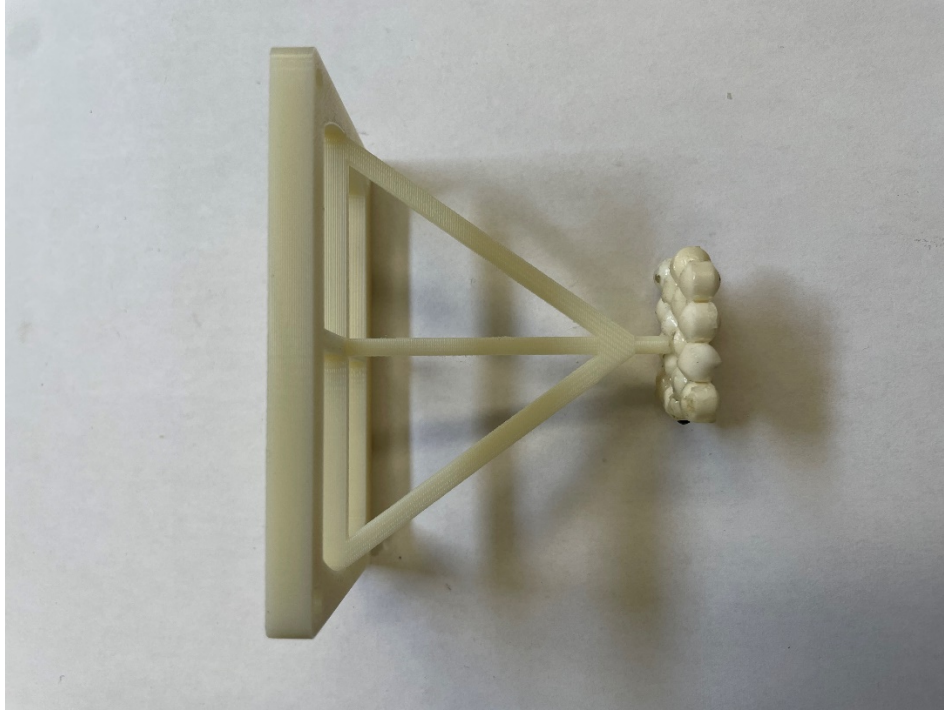


Figure 12. 0.635 cm Al_2O_3 AD995 sample target adhered to target holder.

The impact chamber is bolted to the catch tank. The catch tank is designed to stop and contain all projectiles and fragments after the impact. The catch tank has an I-beam that hangs twenty 0.25" thick mild steel plates placed 1" apart.

For both air and nitrogen, the light gas gun system includes two air compressors (high and low pressure) to enable the compression of both gases to 6000 psi. The high-pressure compressor (Figure 13) compresses and stores the compressed gas into two high pressure double walled storage tanks (Figure 14). The tanks are capable of storing gas at pressures up to 6000 psi.



Figure 13. High pressure compressor. Source: [2].



Figure 14. Dry air storage tanks. Source: [2].

The loading of the compressed air within the gun breech is controlled by a series of computer controlled high pressure electro-pneumatic valves. The computer monitors pressures and controls the filling, firing, and venting within a LabVIEW software program. Figure 15 is a picture of the gun breech and pressure control valves.

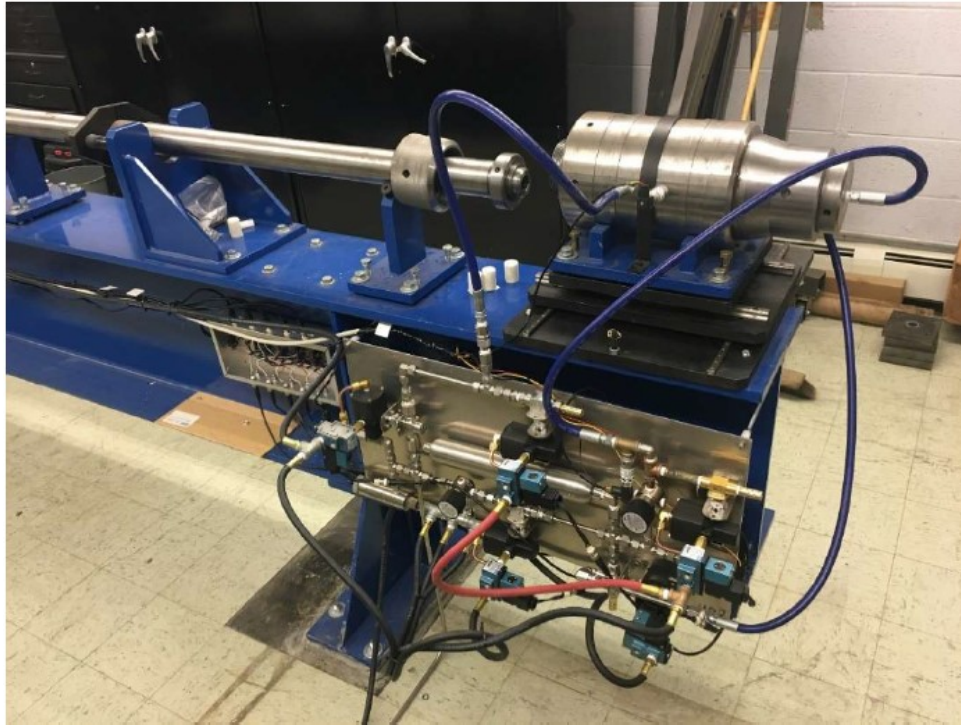


Figure 15. Light gas gun breech and pressure control valves. Source: [1].

4. Video Capturing

Recording of each shot was done using the Shimadzu HPV-2 high-speed video camera as seen in Figure 16. This camera is capable of recording up to 10 Mfps with a 400 x 250-pixel resolution and 30-micron pixel size. This study only used 5 Mfps to capture the entire bullet length for initial and final impact. The camera was positioned perpendicular to the target and projectile flight path. To ensure proper lighting and definition, high intensity LED lighting and a Fresnel lens was used to enable a high intensity backlighting to produce a shadow graph type video. The high intensity

backlighting from the Fresnel lens provided a better contrast within the videos enabling a higher fidelity of tracking within the TEMA software.

The video camera was triggered using a Whithner silver lined break screen (Figure 17). Once the projectile flies through the break screen it opens the connection to the Whithner model 1000 trigger control box in Figure 18. The trigger control box sends a 10V square wave to the Shimadzu camera to begin recording.

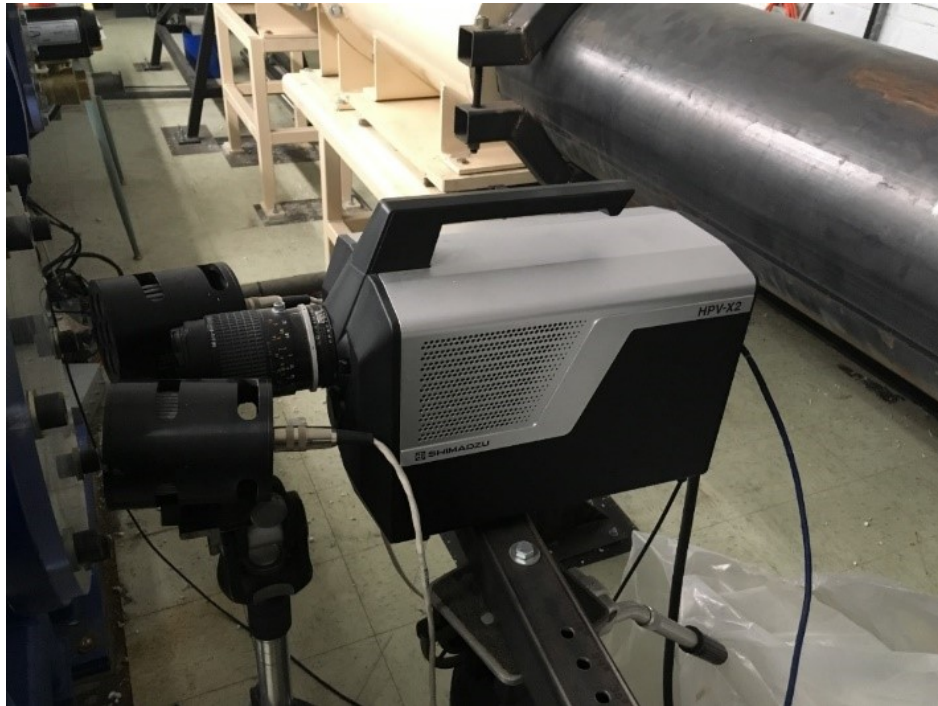


Figure 16. Shimadzu HPV-2 (high-speed video) camera and two LED lights lined up to the port window of the impact chamber. Source: [2].

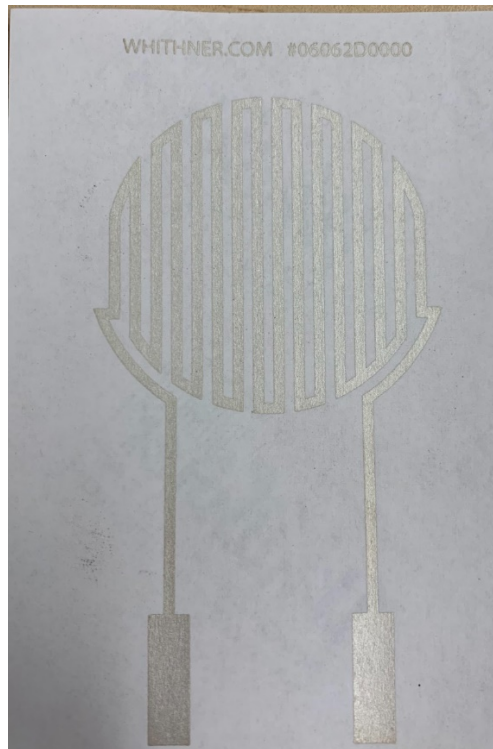


Figure 17. Silver lined break screen.



Figure 18. Trigger control box. Source: [2].

5. Testing Methodology

For this study the light gas gun was shot for each sample type at 5000, 4000, and 3000 psi breech pressures. The sample was attached to the target holder and mounted within the impact chamber. The break screen was attached to the sample target with a thin cardboard standoff. The break screen was wired to the trigger box as a closed circuit. The impact chamber was closed by bolting it to the catch tank.

Once the target sample was mounted, the Shimadzu camera was aligned vertically and horizontally to ensure proper video recording. This also included ensuring the Fresnel lens provided proper lighting to area of interest for the video.

Each shot used the 0.30 caliber M2AP projectile. After the projectile was loaded, the barrel was tightened securely to the breech. Using the LabVIEW program both breech and reset pistons were filled with compressed dry air and the breech was pressurized to the desired firing pressure (5000, 4000, and 3000 psi). Once all safety measures were met, the breech valve was released to launch the projectile down the barrel.

The projectile and sabot traveled down the bore of the barrel to the stripper plate where the sabot was stripped off. The projectile continued into the impact chamber and triggered the break screen. The video camera was then triggered to record and capture the projectile shortly before the impact with the sample; the recording continued though the impact. The video file from the terminal phase was saved and transferred to TEMA for processing.

TEMA is a software program for motion analysis enabling the processing of video files to calculate position, velocity, and acceleration of the projectiles' terminal flights. The program takes into account the camera parameters (frame rate, pixel resolution, focal length, etc.) to provide accurate kinematic data using the known dimensions to scale.

6. TEMA Setup

To properly process the videos, the TEMA program needs to be parameterized with the specifications of the camera setup in use. For the purposes of this thesis camera was parameterized to the following: frame rate was 5 Mfps, gamma of 1.4 - 1.5, focal length of

105 mm, and 32-micron pixel size. The videos are loaded into the program using those specifications.

To scale the images from pixel to meters, a known dimension must be measured. The projectile has a 7.62 mm diameter that was measured in the initial image using to tracking points on the projectile as seen in Figure 19.



Figure 19. TEMA scaling setup.

A third tracker was set up on the back edge of the bullet to track the projectile's motion. The tracking point was placed on the back edge of the projectile, but it was determined that the tracking held better on the corners where there was better pixel resolution for the tracker to hold as seen in Figure 20.

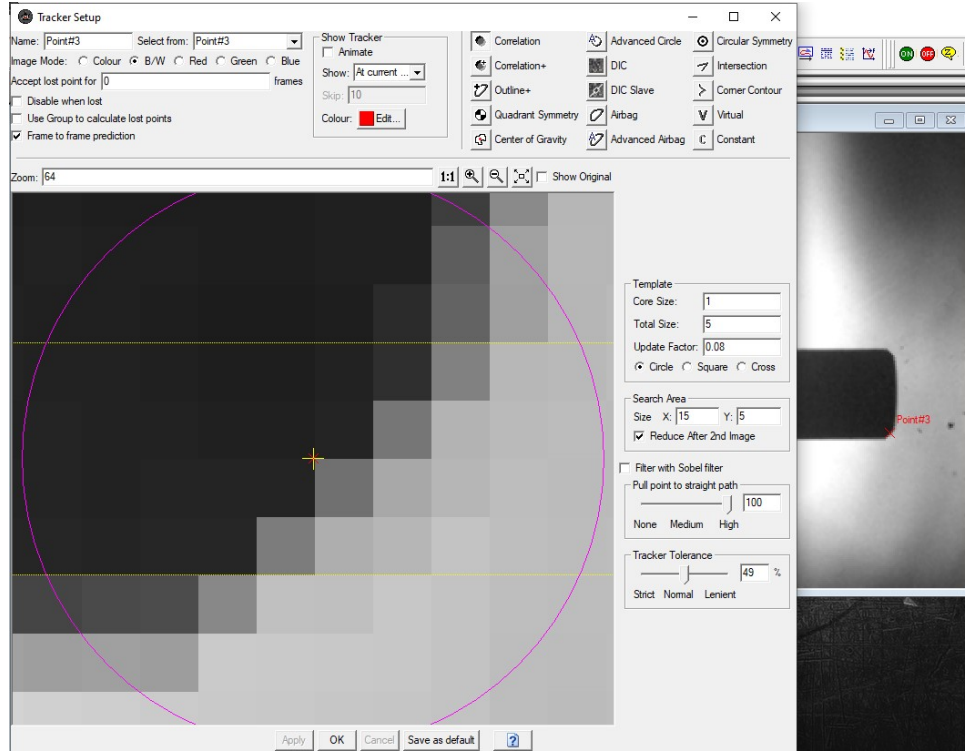


Figure 20. TEMA point three tracker setup.

Tracking from the back edge of the projectile affects the data due to the reverberation from wave motion through the projectile. The reverberations are due to the constant shock wave reflections occurring at both the front and rear boundaries of the projectile. Using Hugoniot equation of state, the shock velocity can be calculated to find the time it takes to propagate compression and rarefaction waves within material. The compression and rarefaction waves for the 0.30 caliber M2AP impacting SiC were calculated to be 6.41 microseconds (μs) for the compression wave and 6.05 μs for the rarefaction wave, combining to a total wave motion through the projectile of 12.46 μs . For the scenario of the 0.30 caliber M2AP impacting AD995, the time for the compression wave was calculated to be 6.31 μs and 5.88 μs for the rarefaction wave, combining to a total wave motion of 12.19 μs through the projectile. Time lag was calculated using a Labview program and the variables listed in Table 5. Results from the Labview program are listed in Table 6. The Labview program uses the following equations

$$U_s = A + bu_p \quad (1)$$

$$\Delta t_{lag} = \frac{\Delta x}{U_s} \quad (2)$$

where U_s is the shock velocity, A & b are experimental accepted Hugoniot values, u_p is the particle velocity, and Δx is the length of the bullet or its core.

Table 5. Hugoniot variables.

Maraging Steel	$\rho = 7.86 \text{ g/cc}$	A = 4.25112 km/s	B = 1.46011
SiC	$\rho = 3.18 \text{ g/cc}$	A = 1.97 km/s	B = 5.18
AD995	$\rho = 4.06 \text{ g/cc}$	A = 3.39 km/s	B = 3.58
Overall Bullet Length	3.556 cm		
Overall Inner AP Core Length	2.8956 cm		
Incident Velocity	650 m/s (~5000 psi)		

Table 6. Hugoniot results from Labview program.

Material	Impact Pressure (GPa)	Projectile (Core) Shock Velocity (m/s)	Particle Velocity (u_p) (m/s)	Δ Time Core Compression Wave (μs)	Δ Time Core Rarefaction Wave (μs)	Δ Time Core Combined (μs)
SiC	6.51	4519	183.3	6.41	6.05	12.46
AD995	8.325	4588	230.75	6.31	5.88	12.19

7. File Output

Once the video plays, the tracker is able to collect data for each image of the video. This data can then be plotted as a single or multi axis graph. In this thesis multi axis plots were used to display position, velocity, and acceleration of the projectile. An example multi and single axis plot is shown in Figure 21. The left image of Figure 24 is a multi-axis graph of position (cyan), velocity (green), and acceleration (red). The right image in Figure 24 is a single axis graph of just velocity. TEMA smooths the data using a set standard deviation. This data has a corresponding timetable that can be exported to Excel. Each sample target video was processed and exported to an Excel spreadsheet.

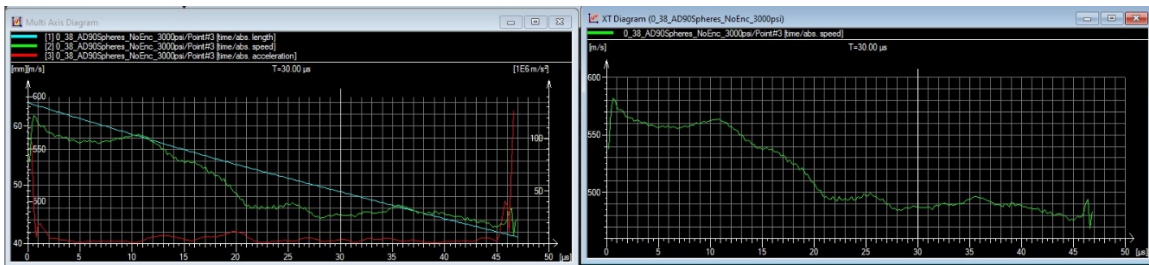


Figure 21. TEMA multi and single axis graphs.

H. DATA PROCESSING

Data from the exported TEMA Excel files were then processed to calculate kinetic energy loss, work performed, and mass efficiency. MATLAB was used to import the TEMA data and make these calculations. Data of position, velocity, and acceleration over time were plotted into graphs for visual comparisons of the samples. Kinetic energy, work, and mass efficiency were calculated then plotted to analyze the samples. Chapter IV and V contain details on the data extracted and analyzed.

Velocity and acceleration were determined in the TEMA software using the positional data collected from the video. The data was smoothed within TEMA using a standard deviation. For this study the frame rate was 5 Mfps, so the time step between frames was $2e-7$ seconds.

Kinetic energy was calculated using the mass of the projectile and change in velocity for each time step. The projectile's mass was 10.57 grams. The following equation was used for kinetic energy,

$$KE = \frac{1}{2}mv^2 \quad (3)$$

where m is the mass of the object and v is the velocity of the object. Kinetic energy loss was calculated using the difference between the maximum kinetic energy subtracted by the minimum kinetic energy, which correlates to the difference between the initial velocity (prior to impact) and final velocity after where the velocity is again constant. Initial velocity and final velocities were apparent in the velocity over time plots where the observed velocities remain constant. Figure 22 displays an example velocity versus time plot from TEMA that shows a mostly stable initial velocity, then decelerates to a mostly stable final velocity. Kinetic energy loss illuminates the loss of velocity due to the sample target. The kinetic energy loss was calculated to compare with work performed by the sample targets against the incident projectile.

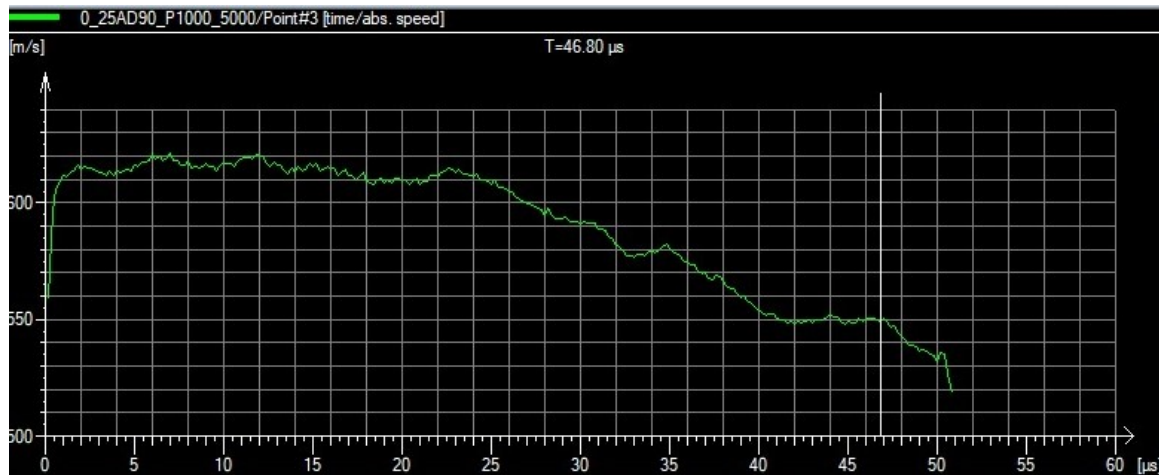


Figure 22. TEMA plot of velocity versus time for ¼" AD90 spheres encapsulated in P1000 shot at 5000 psi. Initial velocity ~ 640 m/s. Final velocity ~ 550 m/s.

Instantaneous work is calculated for each time step using the mass of the projectile, deceleration, and change in position for the specific deceleration calculated. Instantaneous work for a specific time step is calculated using the following equation,

$$\Delta W = ma_{inst}\Delta x \quad (4)$$

where m is the mass of the object, a is the acceleration, and Δx is the change in position. Total work performed was then calculated by adding all the instantaneous works together. Total work was calculated for the time region that correlates to the impact, initial impact to final impact projectile position. Both kinetic energy loss and total work performed are equations for energy lost that can be used to calculate mass efficiency. These calculations explain how much work the target does to the projectile.

Mass efficiency was calculated using the areal density of the material and energy dissipated (energy loss). Table 7 lists the densities and corresponding areal densities of the material used within this study. The areal density is the strength of the material in kilograms per square meter. The equation for mass efficiency is as follows,

$$MassEfficiency = \frac{EnergyDissipated}{ArealDensity} \quad (5)$$

Kinetic energy loss or total work can be used for energy dissipated; I used kinetic energy loss for my calculations. Mass efficiency is used to compare each sample on how efficient it is at stopping the projectile.

Table 7. Density of materials. Sources: [21], [23], [24].

Material	Density [g/cc]	Areal Density [kg/m^2]
SiC	3.04	23.26 (Tile)
Al ₂ O ₃ Alumina 90% Purity (AD90)	3.60	34.74 (Tile) 13.82 (0.635cm Spheres) 20.73 (0.952cm Spheres) 16.32 (0.635cm Spheres with P1000) 24.49 (0.952cm Spheres with P1000)
Al ₂ O ₃ Alumina 99.5% Purity (AD995)	3.90	14.97 (0.635cm Spheres) 22.45 (0.952cm Spheres)
Versalink P1000	0.998	N/A

I. TEST MATRIX

This thesis studies the performance of ceramic spheres using sample targets of approximately four rows where each row incorporates four to five spheres, an example of this is seen in Figure 23. This study also uses sample targets of monolithic ceramic tiles (SiC and Al₂O₃) that were approximately 4” by 4” and 3” by 3” respectively as a control. The purpose of this study is to measure the kinetic energy loss and work performed for each sample target during impact. The ceramic spheres were different combinations of sphere diameter, chemistry, and encapsulation.



Figure 23. Sample target of AD90 ¼” ceramic spheres.

Three sample targets were created for the eight target configurations to test at 5000, 4000, and 3000 psi breech pressures. This consisted of a total of 24 targets. Testing the samples this way enabled comparisons of the sample configurations at each velocity and to measure energy dissipation as a function of velocity. Refer to Table 8.

Six of the eight target configurations were comprised of ceramic spheres with the inclusion of small satellite bands. All of the ceramic spheres were made of alumina (Al_2O_3) but varied between two different purities 90% (AD90) and 99.5% (AD995). Figure 24 displays the different purities; left is 99.5% alumina with more of a yellow hue and right is 90% alumina being a purer white. The ceramic sphere diameter varied between 0.635 cm (1/4 in) and 0.952 cm (3/8 in) as seen in Figure 25. The spheres were also varied between no encapsulation (ultra-flex coating) or Versalink P1000. Figure 26 displays 0.635 cm and 0.952 cm samples encapsulated in P1000, both 90% alumina. The ceramic tiles comprised of alumina of 90% purity and SiC (Saint-Gobain Hexoloy). Table 6 presents the test matrix of all configurations and shots performed.



Figure 24. Al_2O_3 ceramic spheres of different alumina purities. Left is 99.5% alumina; Right is 90% purity.



Figure 25. 0.635 cm and 0.952 cm Al_2O_3 ceramic spheres, both 90% alumina.

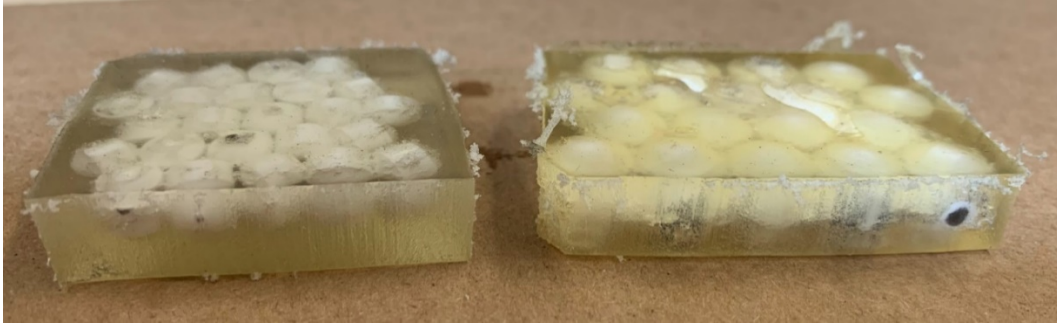


Figure 26. 0.635 cm and 0.952 cm Al_2O_3 ceramic spheres, both 90% alumina and encapsulated in Versalink P1000.

Table 8. Test matrix of shots performed in this study.

Shot #	Target Description	Projectile	Breech Pressure (psi)	Video Frame Rate (FPS)
1	SiC 4" x 4" tile 0.765 cm thickness	0.30 caliber M2AP	5000	5,000,000
2	SiC 4" x 4" tile 0.765 cm thickness	0.30 caliber M2AP	4000	5,000,000
3	SiC 4" x 4" tile 0.765 cm thickness	0.30 caliber M2AP	3000	5,000,000
4	Al ₂ O ₃ AD90 3" x 3" tile 0.952 cm thickness	0.30 caliber M2AP	5000	5,000,000
5	Al ₂ O ₃ AD90 3" x 3" tile 0.952 cm thickness	0.30 caliber M2AP	4000	5,000,000
6	Al ₂ O ₃ AD90 3" x 3" tile 0.952 cm thickness	0.30 caliber M2AP	3000	5,000,000
7	Al ₂ O ₃ AD90 4 Row 0.635 cm sphere no encap	0.30 caliber M2AP	5000	5,000,000
8	Al ₂ O ₃ AD90 4 Row 0.635 cm sphere no encap	0.30 caliber M2AP	4000	5,000,000
9	Al ₂ O ₃ AD90 4 Row 0.635 cm sphere no encap	0.30 caliber M2AP	3000	5,000,000
10	Al ₂ O ₃ AD995 4 Row 0.635 cm sphere no encap	0.30 caliber M2AP	5000	5,000,000
11	Al ₂ O ₃ AD995 4 Row 0.635 cm sphere no encap	0.30 caliber M2AP	4000	5,000,000
12	Al ₂ O ₃ AD995 4 Row 0.635 cm sphere no encap	0.30 caliber M2AP	3000	5,000,000
13	Al ₂ O ₃ AD90 4 Row 0.952 cm sphere no encap	0.30 caliber M2AP	5000	5,000,000
14	Al ₂ O ₃ AD90 4 Row 0.952 cm sphere no encap	0.30 caliber M2AP	4000	5,000,000
15	Al ₂ O ₃ AD90 4 Row 0.952 cm sphere no encap	0.30 caliber M2AP	3000	5,000,000
16	Al ₂ O ₃ AD995 4 Row 0.952 cm sphere no encap	0.30 caliber M2AP	5000	5,000,000
17	Al ₂ O ₃ AD995 4 Row 0.635 cm sphere no encap	0.30 caliber M2AP	4000	5,000,000
18	Al ₂ O ₃ AD995 4 Row 0.635 cm sphere no encap	0.30 caliber M2AP	3000	5,000,000
19	Al ₂ O ₃ AD90 4 Row 0.635 cm sphere P1000	0.30 caliber M2AP	5000	5,000,000
20	Al ₂ O ₃ AD90 4 Row 0.635 cm sphere P1000	0.30 caliber M2AP	4000	5,000,000
21	Al ₂ O ₃ AD90 4 Row 0.635 cm sphere P1000	0.30 caliber M2AP	3000	5,000,000
22	Al ₂ O ₃ AD90 4 Row 0.952 cm sphere P1000	0.30 caliber M2AP	5000	5,000,000
23	Al ₂ O ₃ AD90 4 Row 0.952 cm sphere P1000	0.30 caliber M2AP	4000	5,000,000
24	Al ₂ O ₃ AD90 4 Row 0.952 cm sphere P1000	0.30 caliber M2AP	3000	5,000,000

THIS PAGE INTENTIONALLY LEFT BLANK

IV. DATA

Kinematic data for each sample was calculated using TEMA. The exported data was plotted as a function of time for all sample targets and incident velocities. Data starts prior to impact and continues through impact of the 0.30 caliber M2AP until a post impact constant velocity is observed. The plots identify position, velocity, and acceleration changes verses time for each sample.

J. POSITION VS. TIME

Position of the back of the projectile, as a function of time, during the impact are presented in Figures 27–29. Each figure presents the position changes for different velocities correlated to breech pressures of 5000psi, 4000psi, and 3000psi respectively. The slope of the data describes how rapidly the position changes occur for each of the sample target systems. The instantaneous change in position was used to calculate work performed on the projectile by each of the eight sample targets.

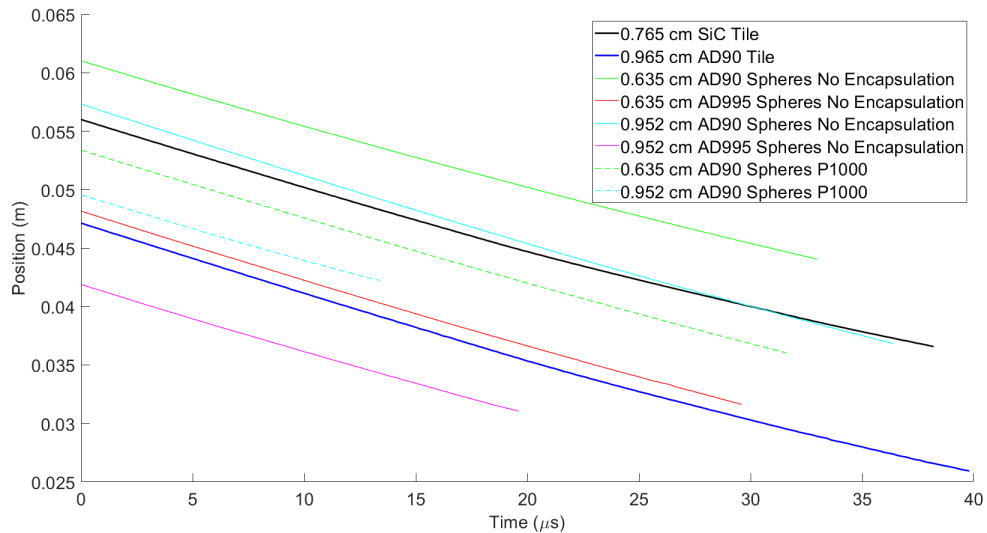


Figure 27. Position vs. time at breech pressure of 5000 psi for each of the eight sample targets.

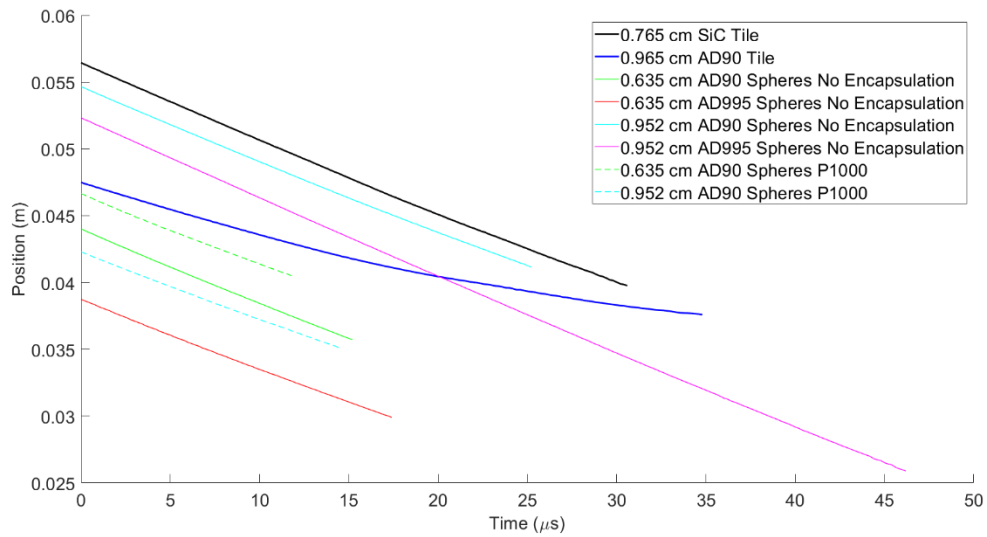


Figure 28. Position vs. time at breech pressure of 4000 psi for each of the eight sample targets.

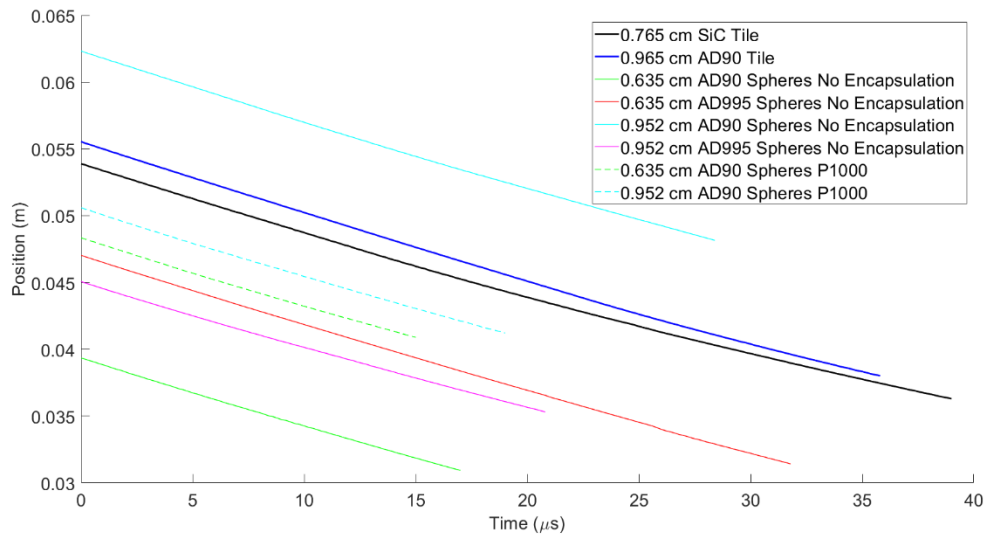


Figure 29. Position vs. time at breech pressure of 3000 psi for each of the eight sample targets.

K. VELOCITY OVER TIME

The velocity changes of the projectile verses time during the ballistic impact are presented for the eight different targets at the three different breech pressures. Figures 30–

32 display the velocity dependence verses time of the projectile at the three different breech pressures (5000 psi, 4000 psi, and 3000 psi). Data presents a mostly steady initial velocity prior to impact, then a drop in velocity until a final constant velocity is observed after complete penetration. This difference in projectile velocity was used to calculate kinetic energy loss for each sample. The ripples in the data are due to the oscillations of wave motion within the projectile.

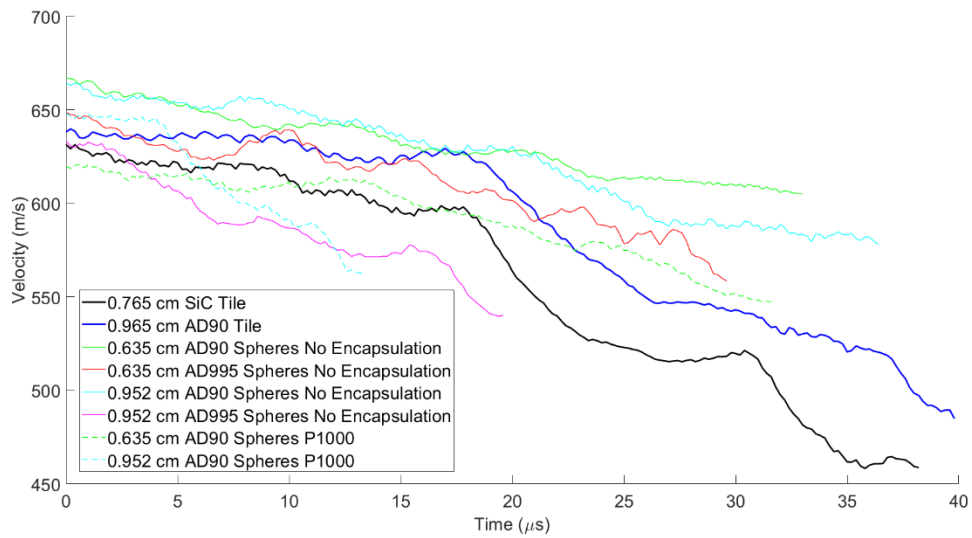


Figure 30. Velocity vs. time at breech pressure 5000 psi for each of the eight sample targets.

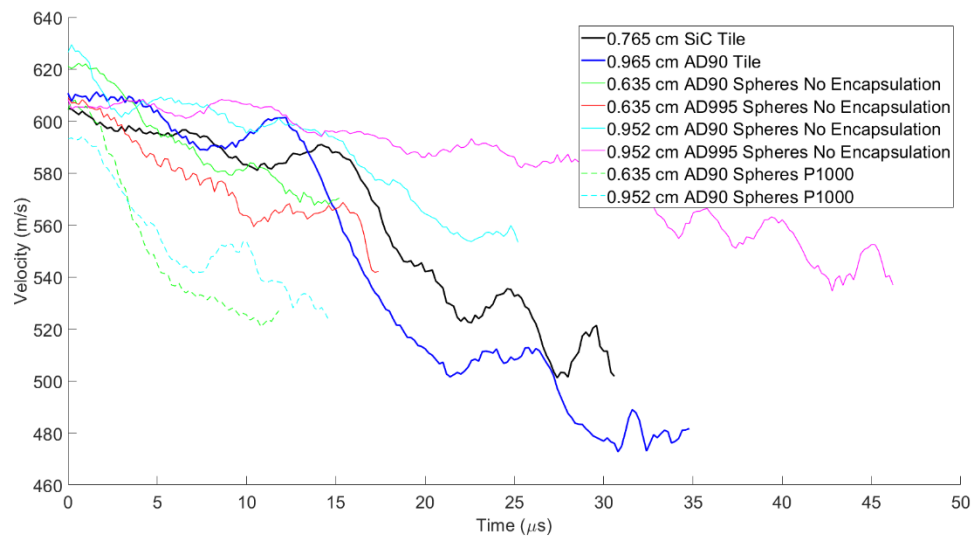


Figure 31. Velocity vs. time at breech pressure 4000 psi for each of the eight sample targets

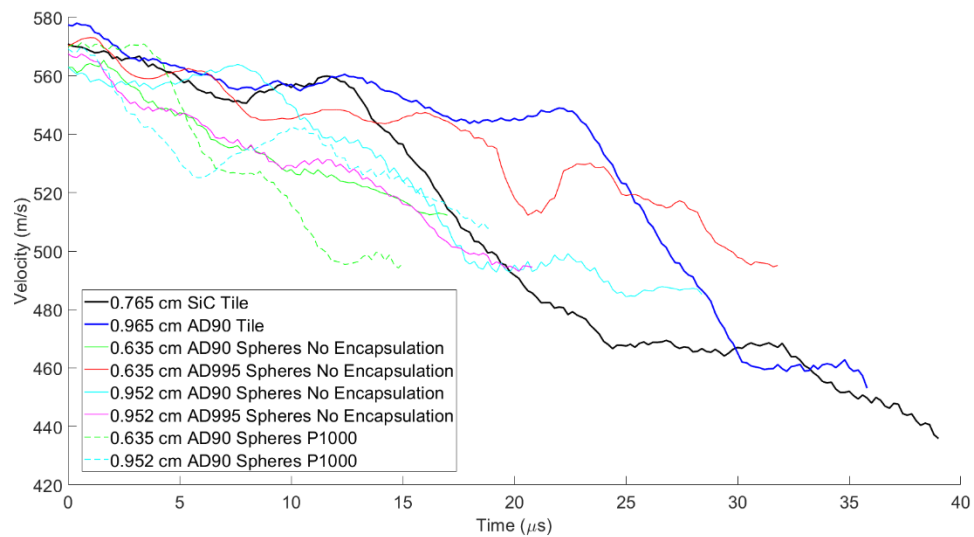


Figure 32. Velocity vs. time at breech pressure 3000 psi for each of the eight sample targets

L. ACCELERATION OVER TIME

The acceleration changes of the projectile vs. time, during the impact, are presented for the eight different targets at the three breech pressures. Figures 33–35 display the velocity dependence vs. time of the projectile at three different initial breech pressures (5000 psi, 4000 psi, and 3000 psi). The acceleration was also used to calculate work performed by the target on the incident projectile.

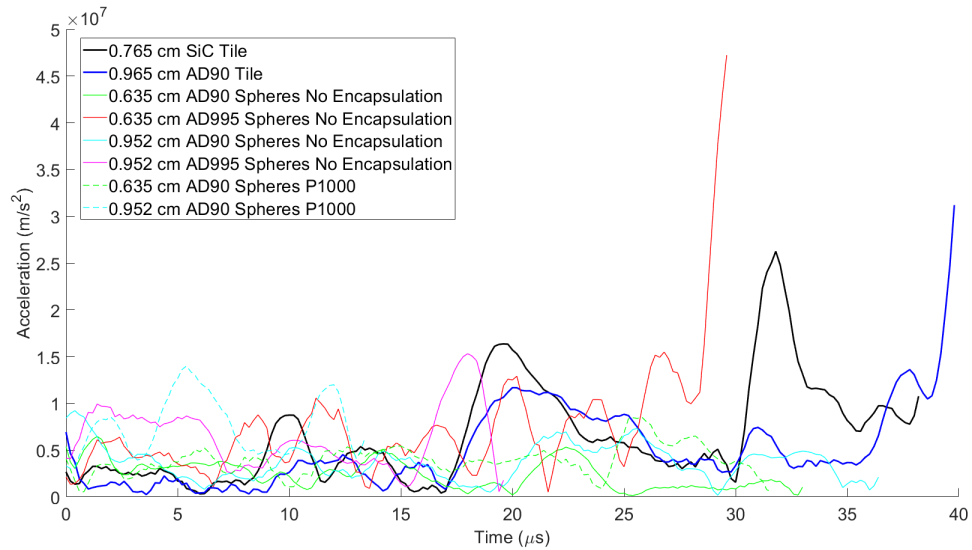


Figure 33. Acceleration vs. time at breech pressure of 5000 psi for each of the eight sample targets.

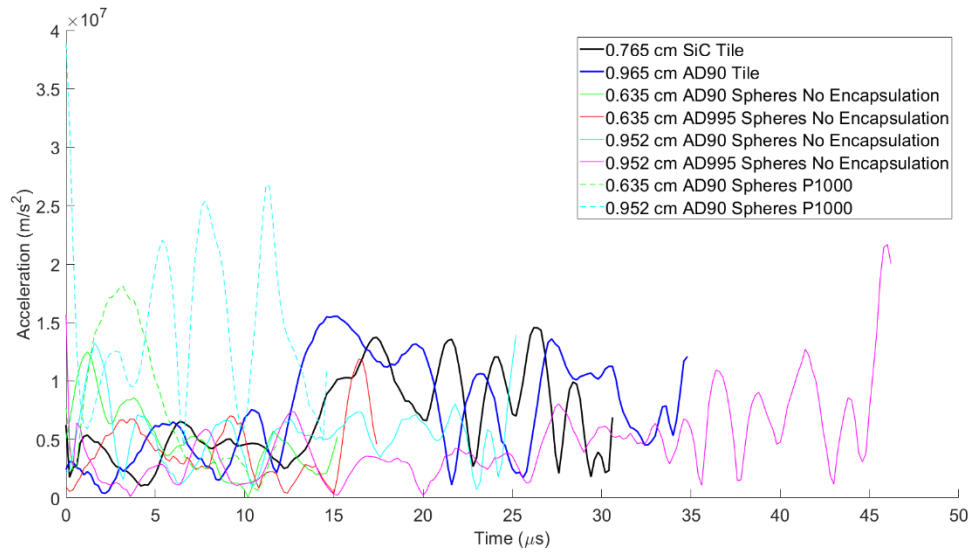


Figure 34. Acceleration vs. time at breech pressure of 4000 psi for each of the eight sample targets.

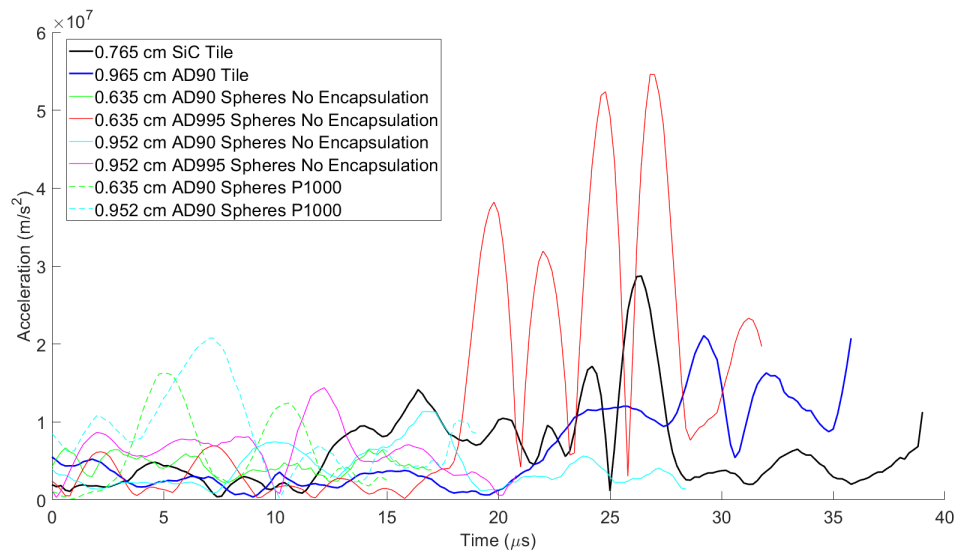


Figure 35. Acceleration vs. time at breech pressure of 3000 psi for each of the eight sample targets.

V. DATA ANALYSIS

Kinematic data from Chapter IV was analyzed for instantaneous work, kinetic work dissipation, work summation, kinetic energy loss, total work, and mass efficiency. The data was used to compare how effective each sample performed stopping the 0.30 caliber M2AP projectile.

M. INSTANTANEOUS WORK VS. TIME

Instantaneous work was calculated for each sample using equation (4). These calculations included the summation of the instantaneous force multiplied by the distance traveled within each time step of the projectile. These plots display the work performed by the eight sample targets as a function of time.

Figure 36 compares the instantaneous work as a function of time for each sample. The 0.635 cm AD995 with no encapsulation has the highest peak work, but the SiC tile has more positive work over the entire impact. The work each sample does to the projectile occurs in periods of increased, decreased, and no work done throughout the impact.

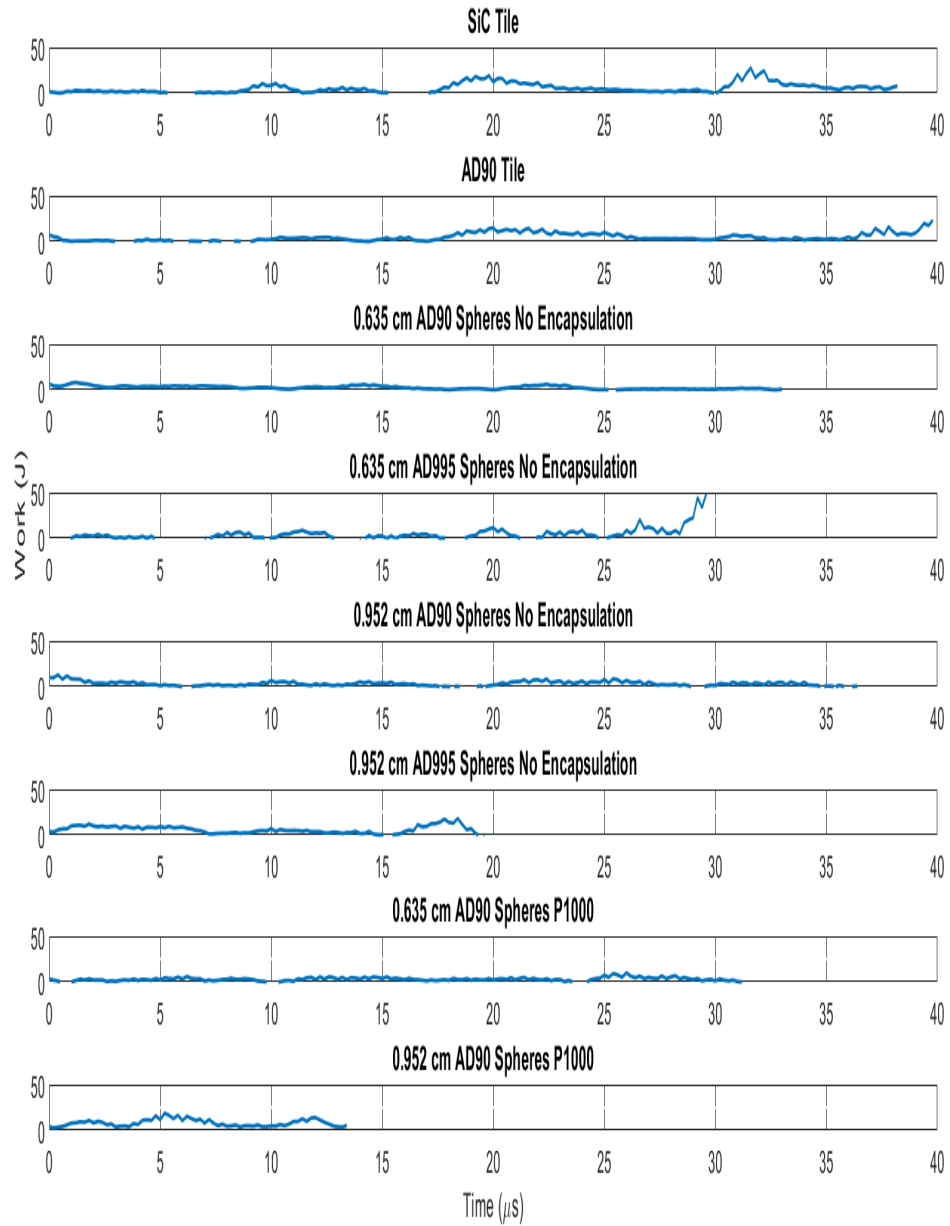


Figure 36. Instantaneous work vs. time at breech pressure 5000 psi for the eight sample targets.

Figure 37 compares the work verses time for an AD90 tile, 0.635 and 0.952 cm diameter spheres including both with and without polymer encapsulation (P1000). The

AD90 tile performed the highest work on the incident projectile. The encapsulated and non-encapsulated 0.635 cm AD90 spheres appear to do a similar amount of work (encapsulation does not appear to contribute to the penetration resistance performance). The 0.952 cm encapsulated AD90 spheres demonstrate increased work and over a shorter amount of time. The 0.952 cm spheres perform more work than the 0.635 cm spheres which is very apparent in the encapsulated samples.

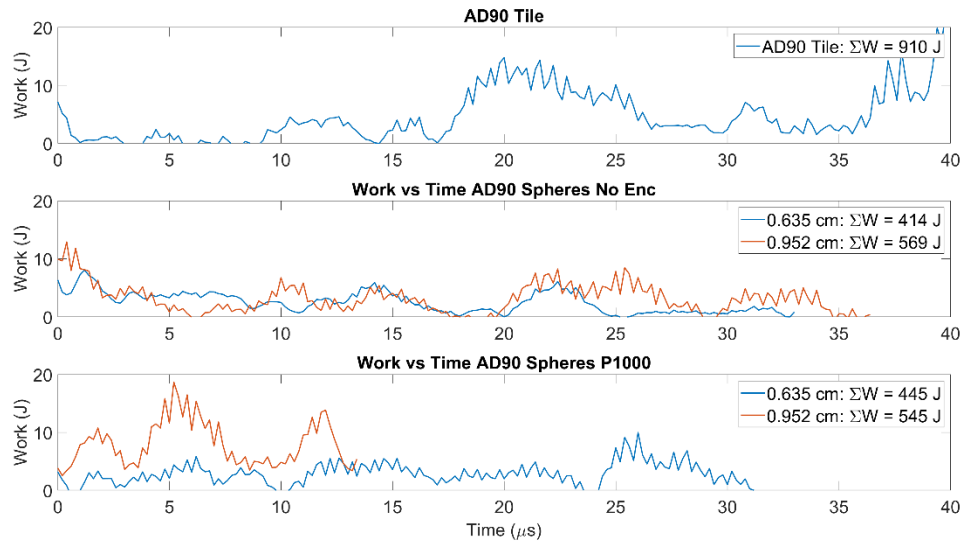


Figure 37. Instantaneous work vs. time at breech pressure 5000 psi for AD90.

Figure 38 displays the work done by the 0.635 cm spheres and 0.952 cm spheres for both AD90 and AD995 chemistries. The AD995 spheres outperformed the AD90 spheres for both the diameters, but it was more apparent in the 0.635 cm spheres. The 0.952 cm AD995 sphere system both performed more work and performed the work in a shorter period of time compared to other ceramic spheres.

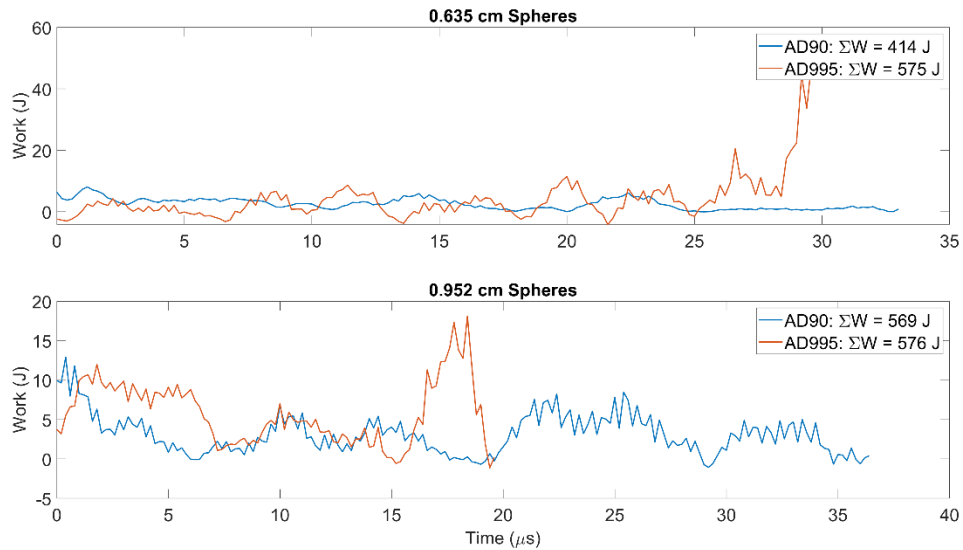


Figure 38. Instantaneous work vs. time at breech pressure 5000 psi for AD90 vs. AD995 spheres.

N. KINETIC ENERGY DISSIPATED/WORK SUMMATION OVER TIME

Figures 39–46 display how the kinetic energy decreases over time as well as how the work increases over time for each sample respectively. The kinetic energy will dissipate at the initial velocity is higher than the final velocity. Work will increase over time as total work is a summation of the work performed during each time step. These plots display the rate at which the samples react to the projectile and perform the work to slow/stop the impact. This is important to see when the sample does the work during the impacts. The kinetic energy dissipation and work summation follow a similar trend for each target.

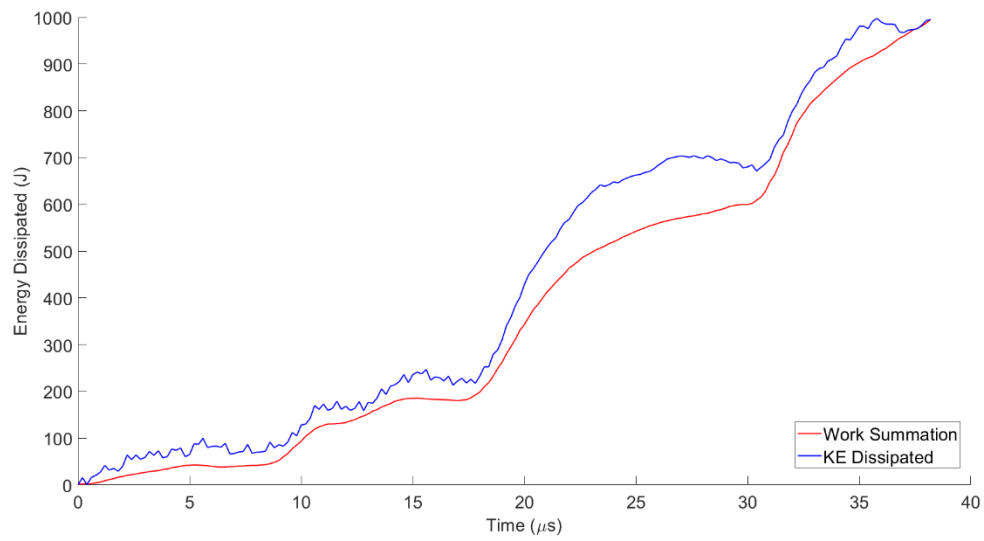


Figure 39. Kinetic energy dissipation and work summation vs. time at breech pressure 5000 psi for SiC tile.

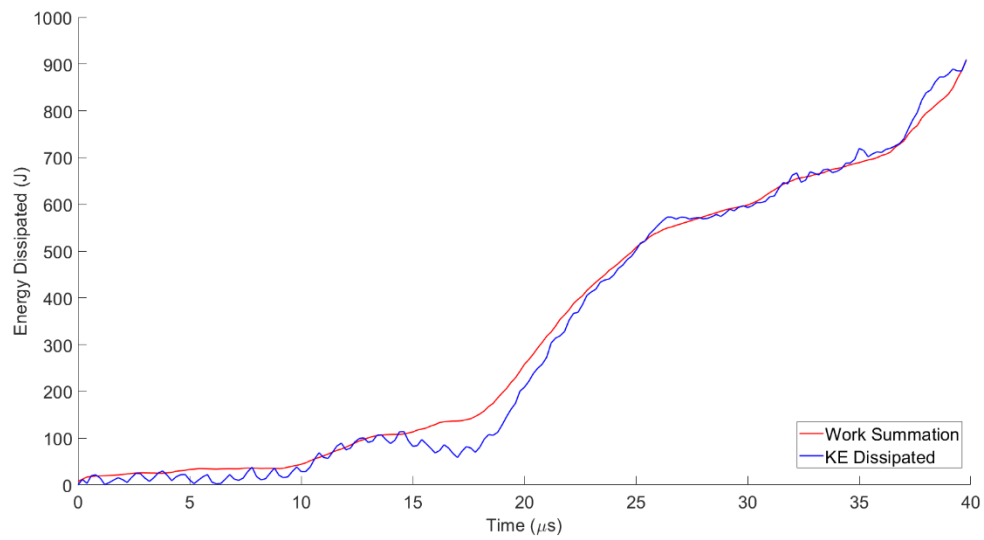


Figure 40. Kinetic energy dissipation and work summation vs. time at breech pressure 5000 psi for AD90 tile.

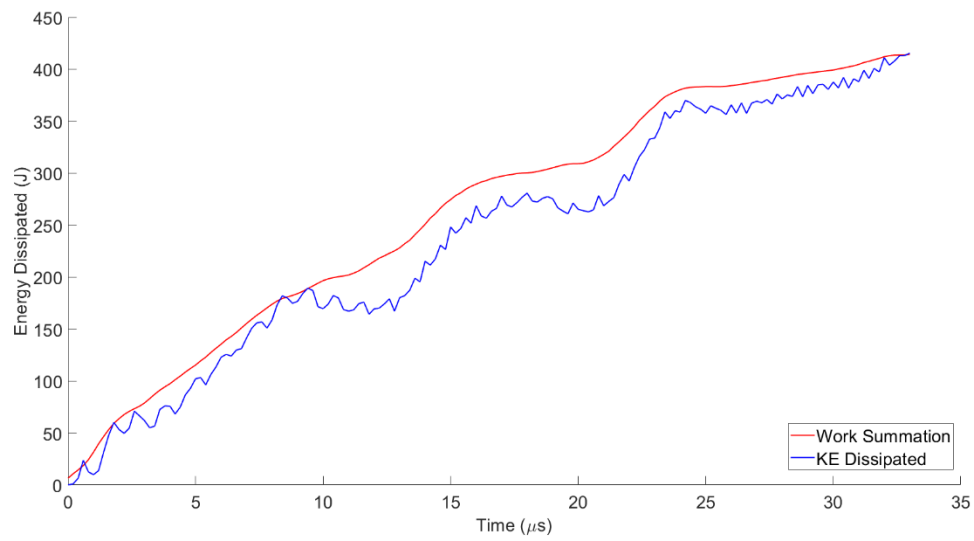


Figure 41. Kinetic energy dissipation and work summation vs. time at breech pressure 5000 psi for 0.635 cm AD90 spheres no encapsulation.

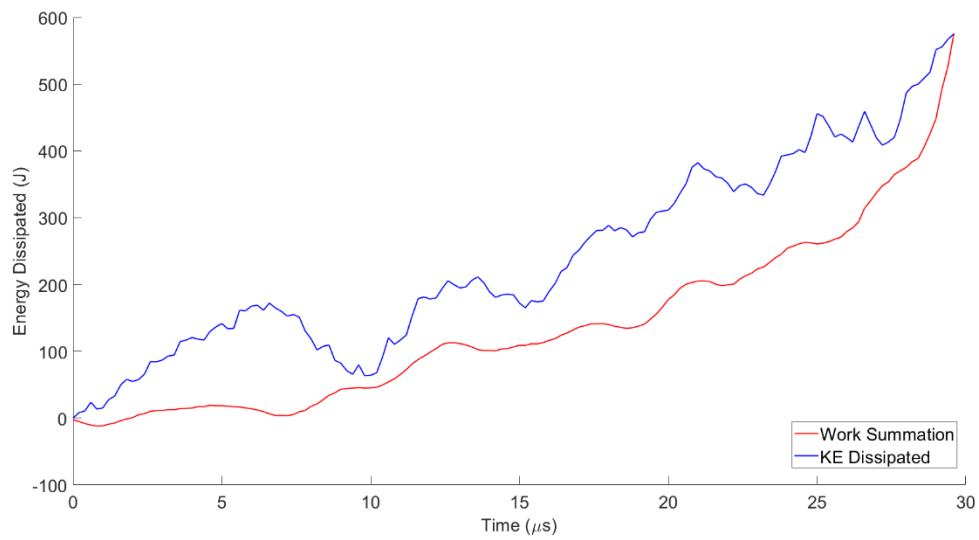


Figure 42. Kinetic energy dissipation and work summation vs. time at breech pressure 5000 psi for 0.635 cm AD995 spheres no encapsulation.

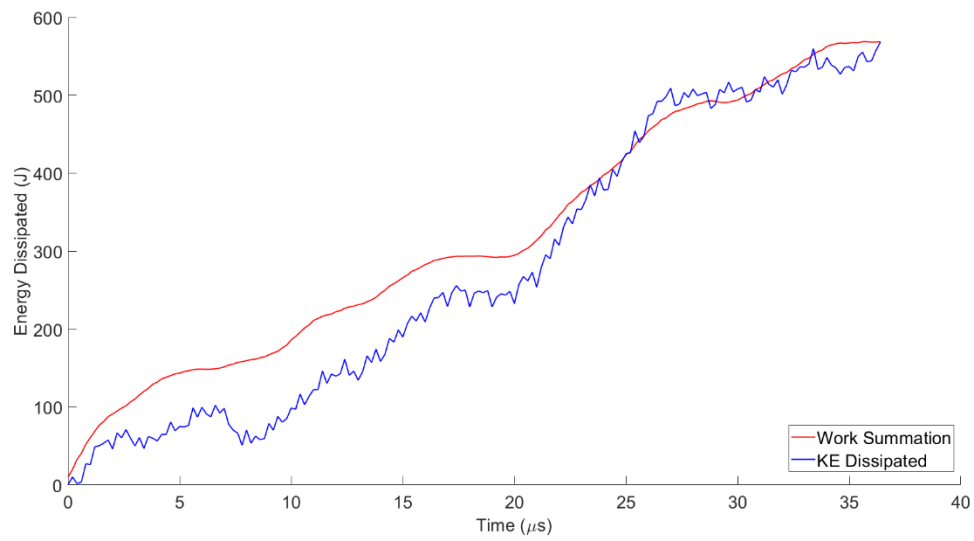


Figure 43. Kinetic energy dissipation and work summation vs. time at breech pressure 5000 psi for 0.952 cm AD90 spheres no encapsulation.

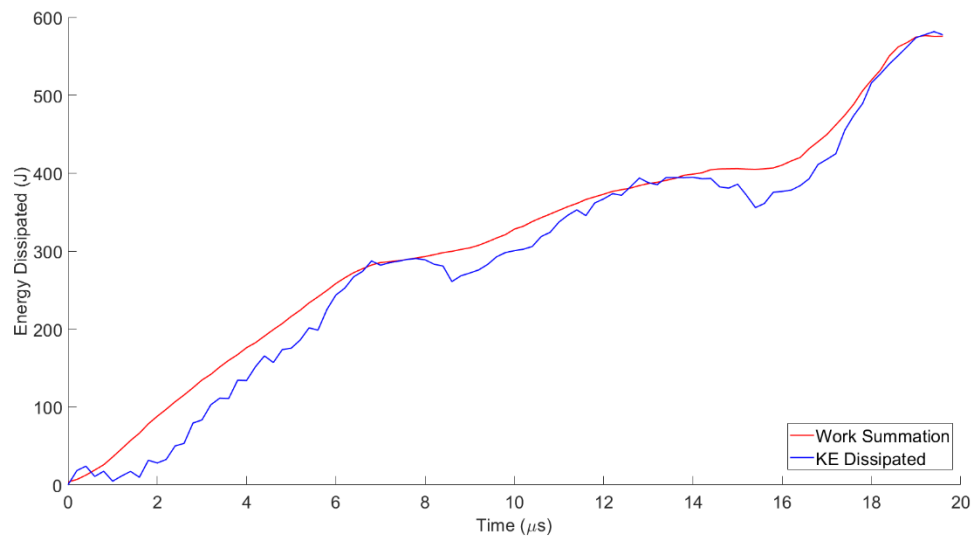


Figure 44. Kinetic energy dissipation and work summation vs. time at breech pressure 5000 psi for 0.952 cm AD995 spheres no encapsulation.

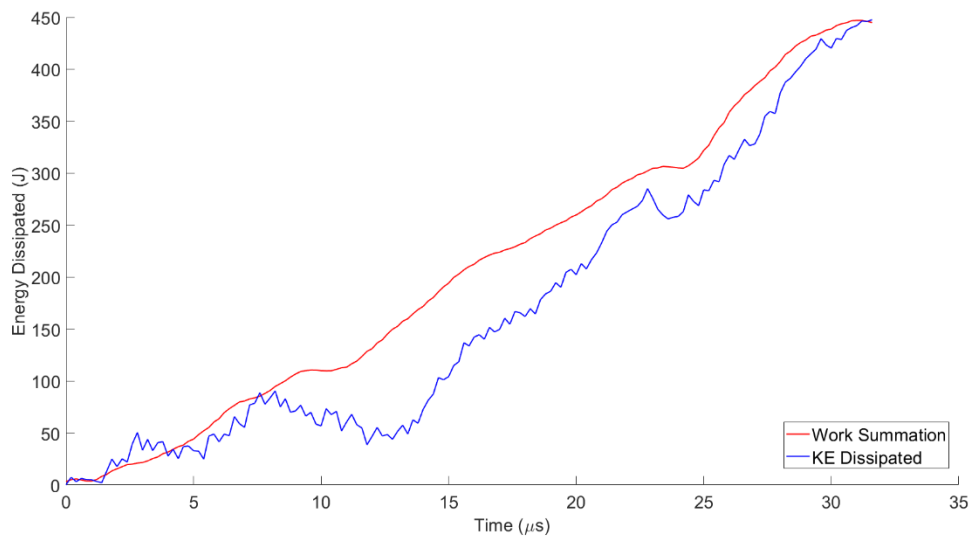


Figure 45. Kinetic energy dissipation and work summation vs. time at breech pressure 5000 psi for 0.635 cm AD90 spheres encapsulated in P1000.

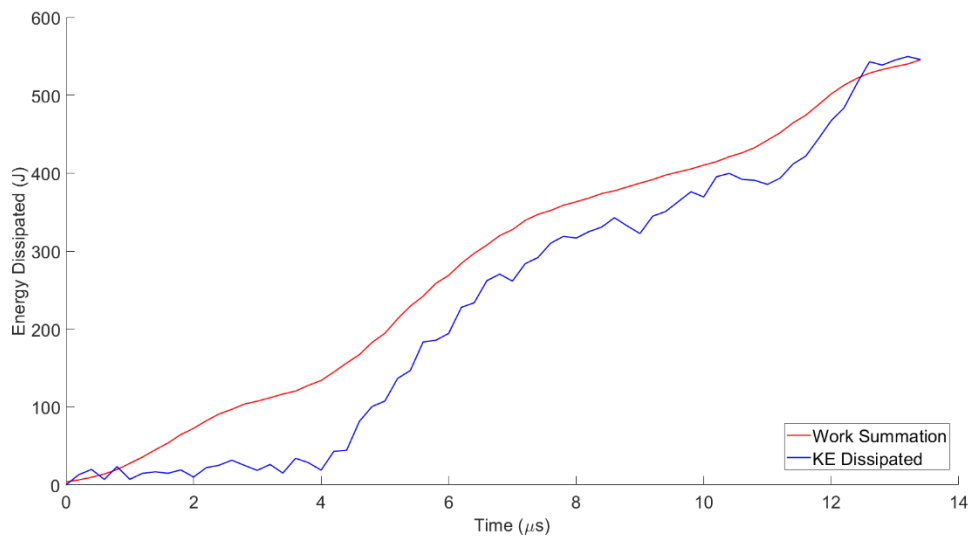


Figure 46. Kinetic energy dissipation and work summation vs. time at breech pressure 5000 psi for 0.952 cm AD90 spheres encapsulated in P1000.

Figures 47 and 48 are plots of the kinetic energy dissipation and work summation over time for all the samples at 5000 psi breech pressure respectively. It is apparent that the tiles (SiC and AD90) perform more kinetic energy loss and work than the other sample, but the SiC tile does more work at the end than the AD90 tile. All samples follow a similar

trend of a steep slope of work done initially then it tapers off towards the end while continuing to do work against the projectile.

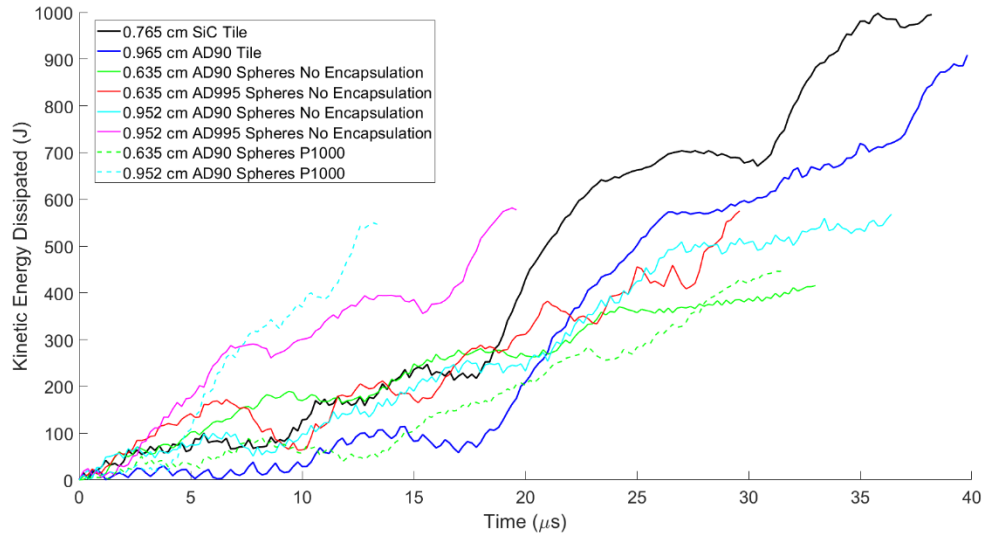


Figure 47. Kinetic energy dissipation vs. time at breech pressure 5000 psi for all eight sample targets.

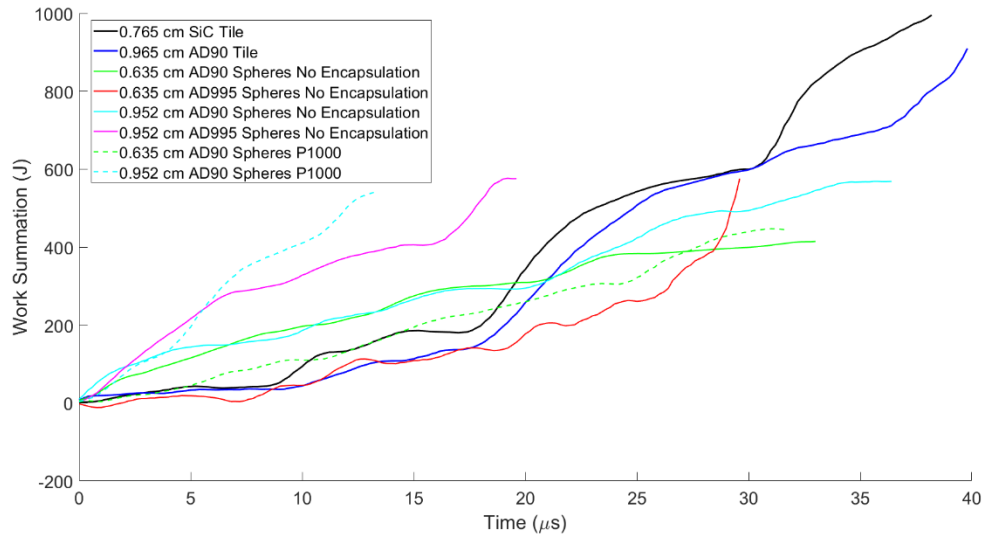


Figure 48. Work summation vs. time at breech pressure 5000 psi for all eight sample targets.

O. INSTANTANEOUS KINETIC ENERGY AND WORK VS. TIME

Figures 49–56 display the instantaneous kinetic energy and work verses time. Both the instantaneous kinetic energy and work follow a similar pattern. These plots provide a deeper understanding of when and how much work is being performed by the sample targets. Some of the intervals in the plots correlate with the Hugoniot results of wave motion times listed in Table 6. Table 6 provides a rough guideline to the timing of the compression and rarefaction waves propagating through the projectile after initial impact. The compression and rarefaction waves are observed in Figures 49–56 by the two large peaks towards the end of the impact. Specifically looking at Figure 49, the peaks occur at 19.6 and 31.8 μs for a total time of 12.2 μs . The total wave motion time predicted in Table 6 was 12.46 μs for SiC proving what we are observing in Figure 49 is the compression and rarefaction waves. This also proves the core of the projectile remains intact during the ballistic impact. The SiC and AD90 tiles appear to have two large peak intervals of work where the sphere targets tend to have three large peak intervals.

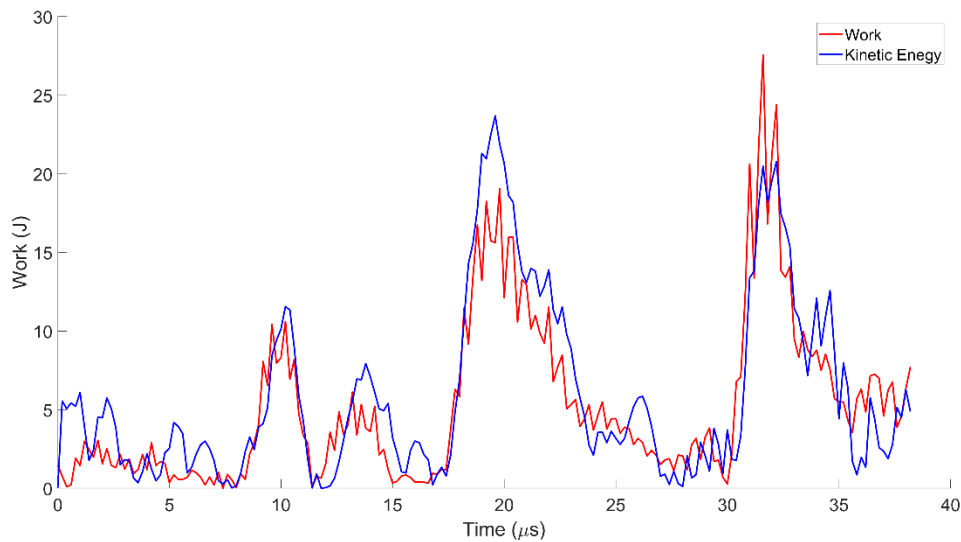


Figure 49. Instantaneous kinetic energy and work vs. time for SiC tile at 5000 psi.

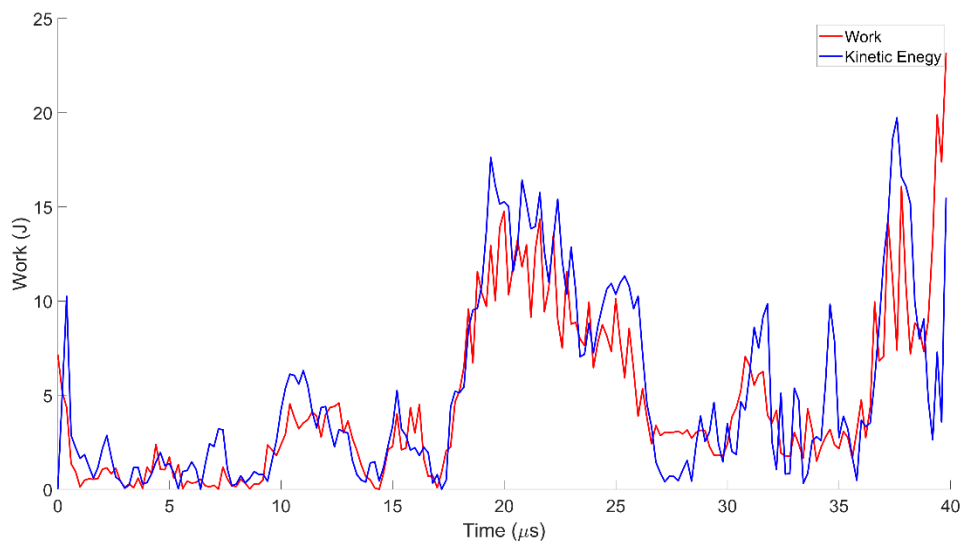


Figure 50. Instantaneous kinetic energy and work vs. time for AD90 tile at 5000 psi.

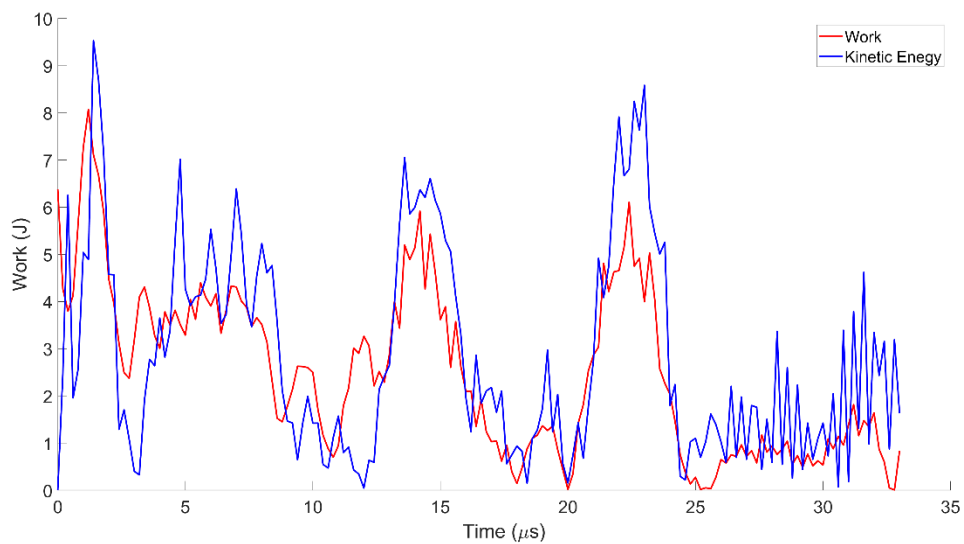


Figure 51. Instantaneous kinetic energy and work vs. time for 0.635 cm AD90 spheres no encapsulation at 5000 psi.

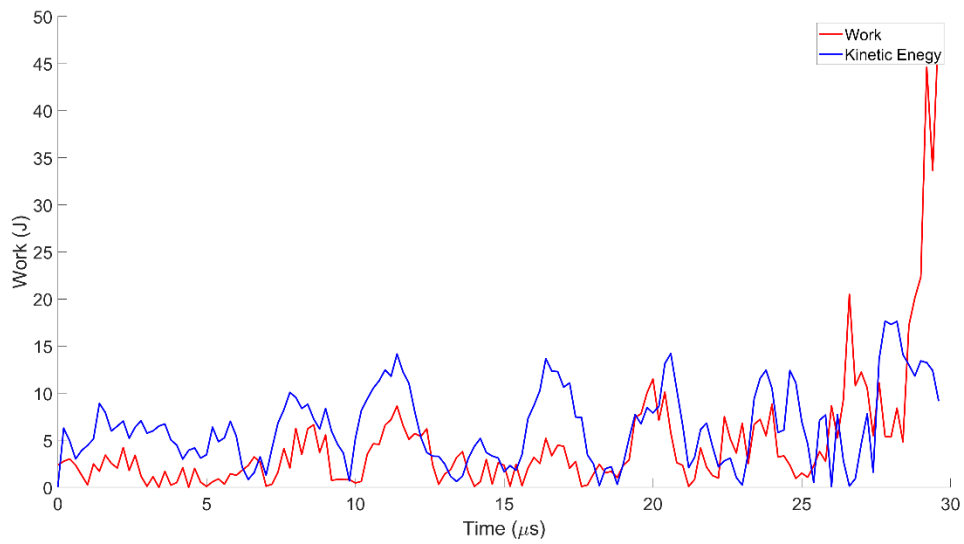


Figure 52. Instantaneous kinetic energy and work vs. time for 0.635 cm AD995 spheres no encapsulation at 5000 psi.

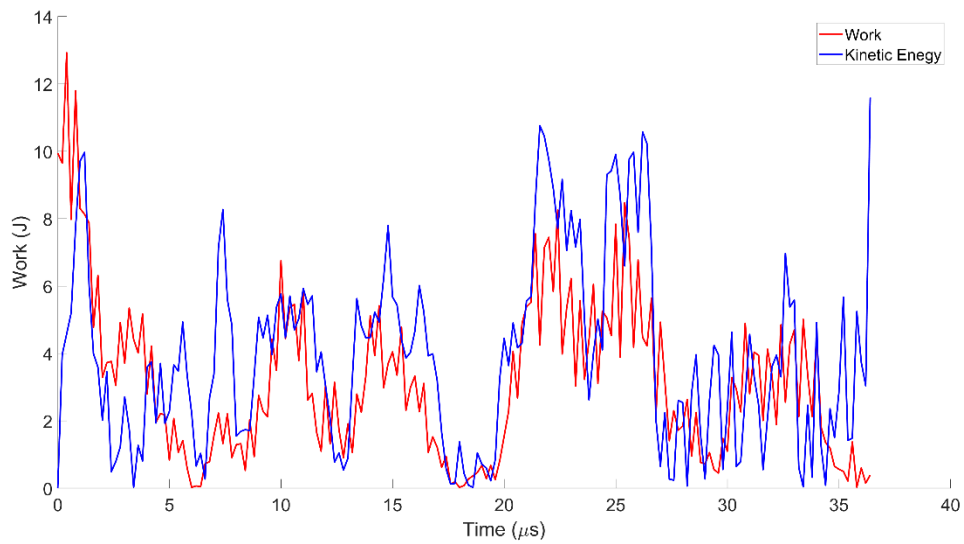


Figure 53. Instantaneous kinetic energy and work vs. time for 0.952 cm AD90 spheres no encapsulation at 5000 psi.

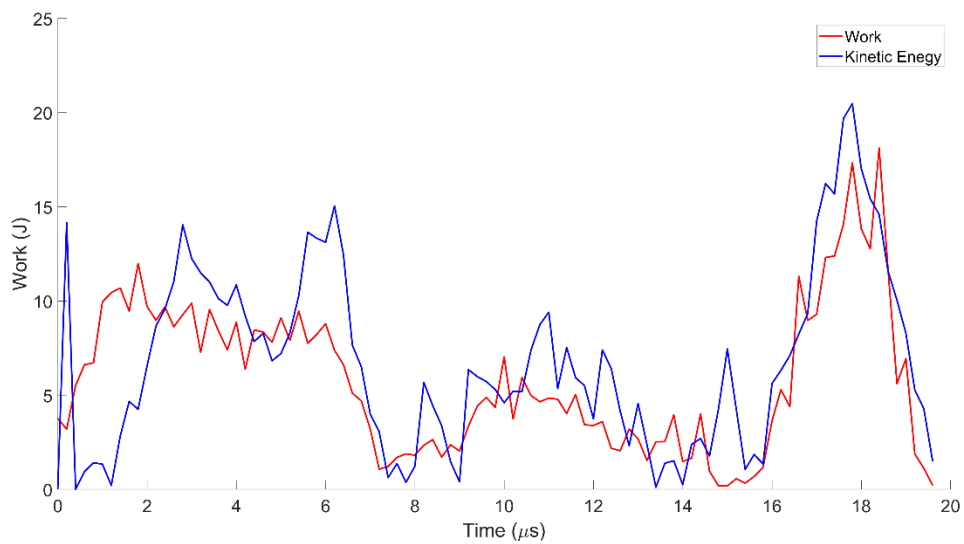


Figure 54. Instantaneous kinetic energy and work vs. time for 0.635 cm AD995 spheres no encapsulation at 5000 psi.

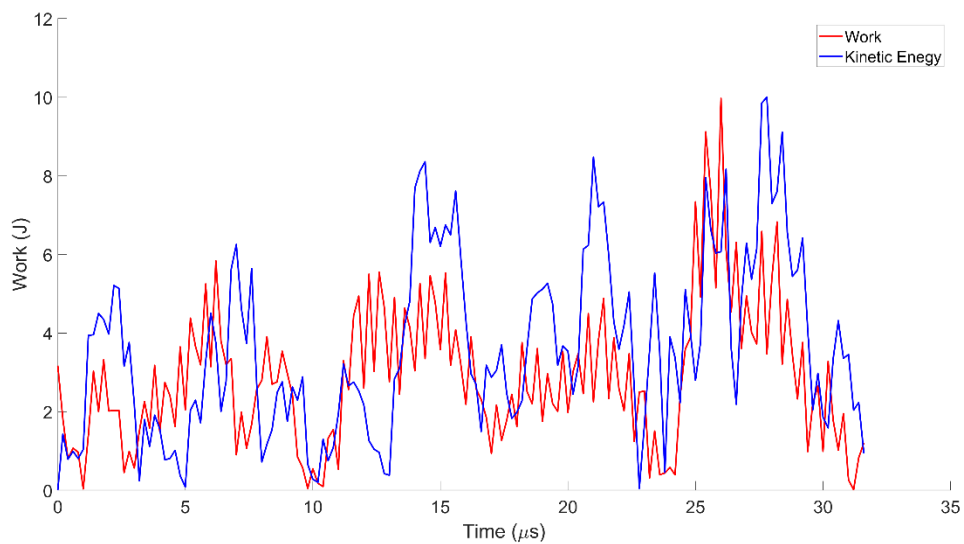


Figure 55. Instantaneous kinetic energy and work vs. time for 0.635 cm AD90 spheres encapsulated in P1000 at 5000 psi.

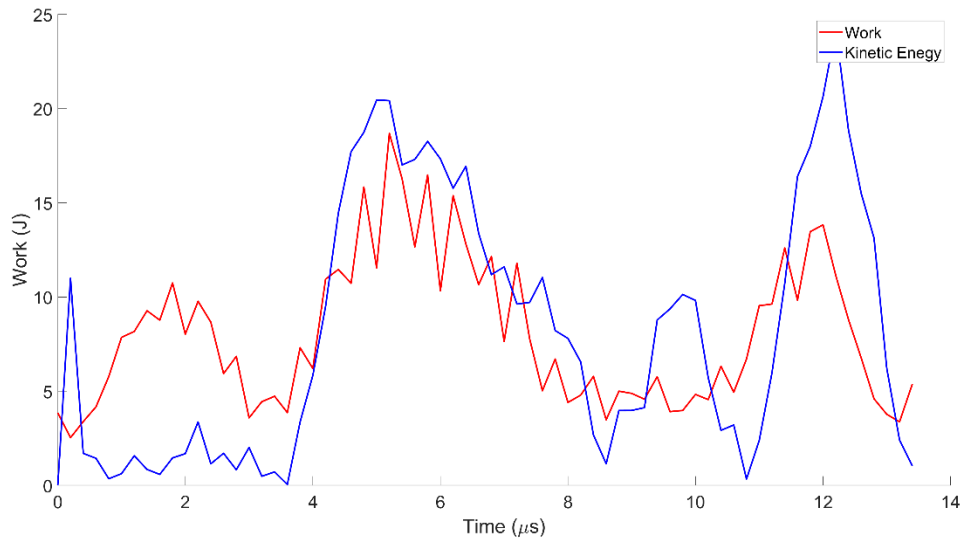


Figure 56. Instantaneous kinetic energy and work vs. time for 0.952 cm AD90 spheres encapsulated in P1000 at 5000 psi.

P. KINETIC ENERGY LOSS AND TOTAL WORK

Figures 57–64 display the kinetic energy loss and total work done by each sample as a function of impact velocity (breach pressure). The impact velocities correlate to the breach pressures at 3000, 4000, and 5000 psi. Kinetic energy loss was calculated using equation 3 that accounts for the mass of the projectile as well as the initial and final speed of the projectile prior to and after impact of the sample target. Calculation of the total work sums all of the instantaneous work performed by the target samples. Each plot shows both an increase in kinetic energy lost by the projectile and total work performed by the sample. Additionally, the amount of kinetic energy lost by the projectile and total work performed by the target sample are self-consistent.

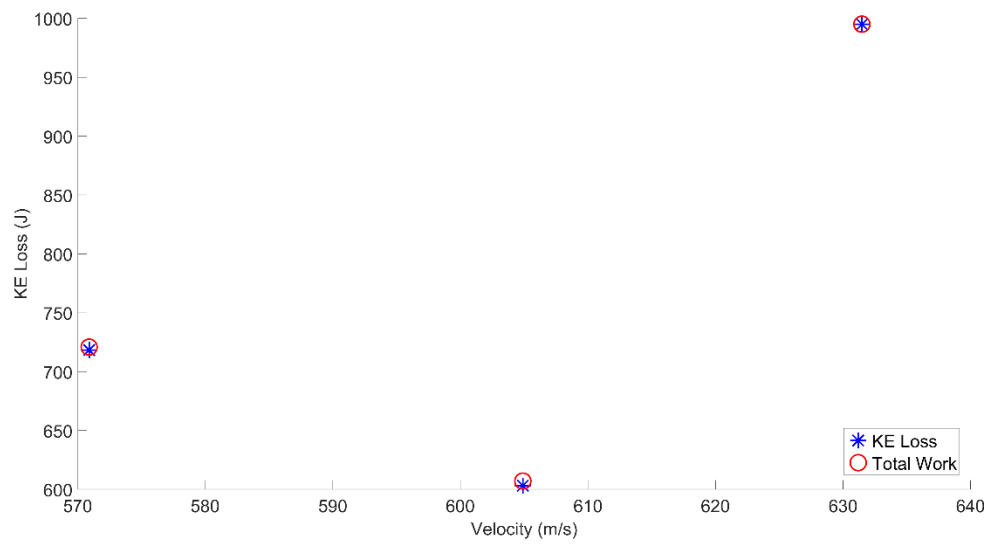


Figure 57. Kinetic energy loss vs. velocity for SiC tile.

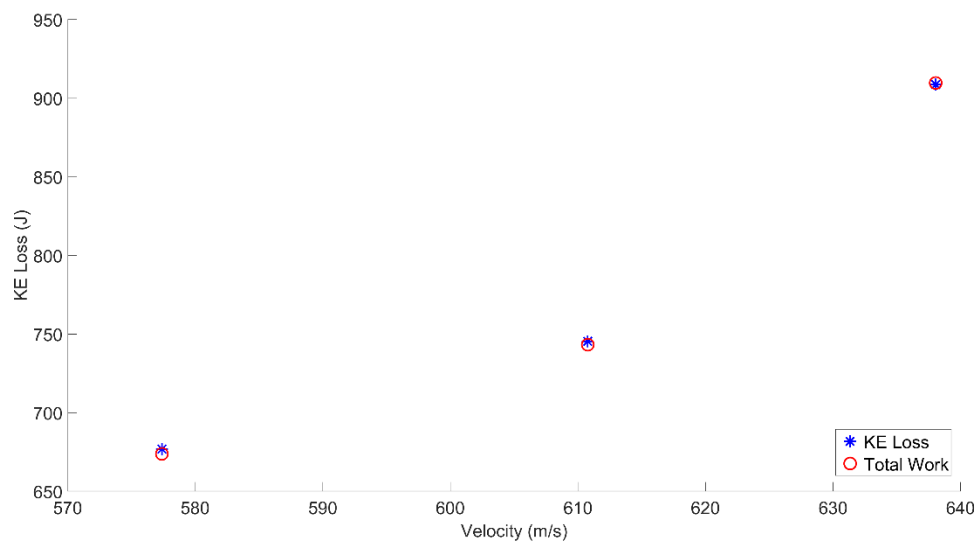


Figure 58. Kinetic energy loss vs. velocity for AD90 tile.

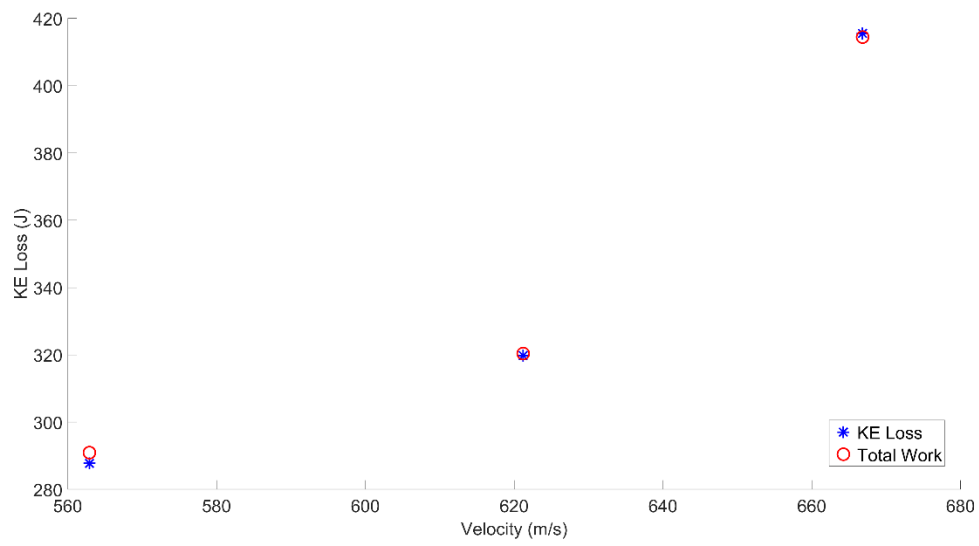


Figure 59. Kinetic energy loss vs. velocity for 0.635 cm AD90 spheres no encapsulation.

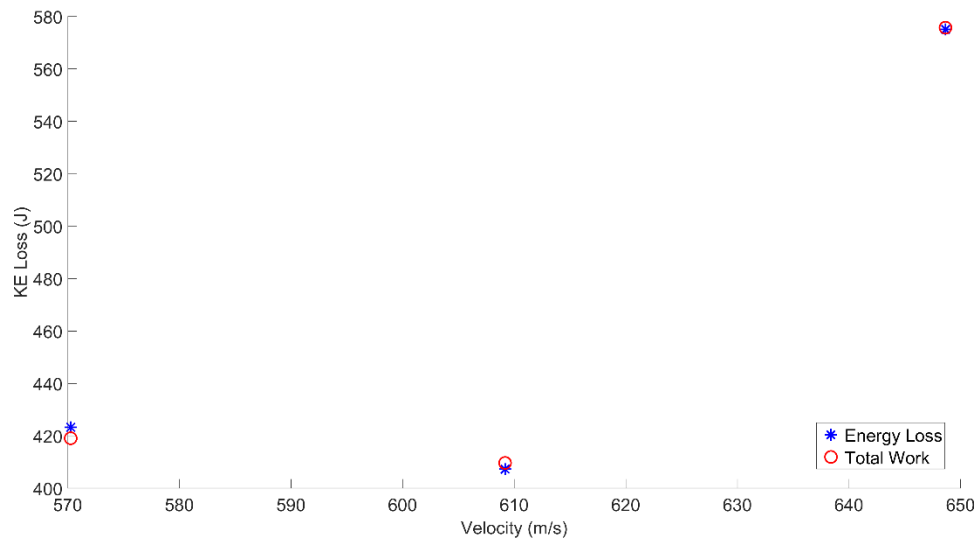


Figure 60. Kinetic energy loss vs. velocity for 0.635 cm AD995 spheres no encapsulation.

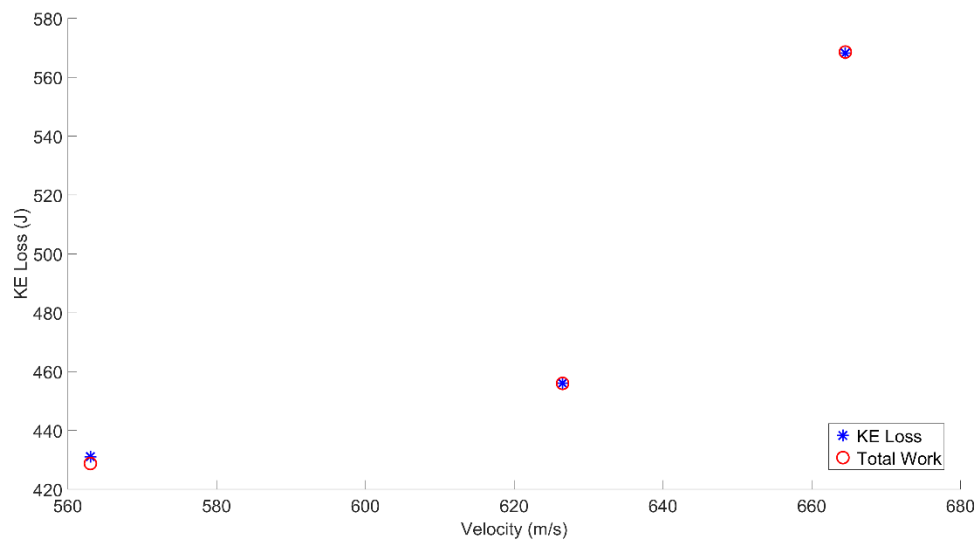


Figure 61. Kinetic energy loss vs. velocity for 0.952 cm AD90 spheres no encapsulation.

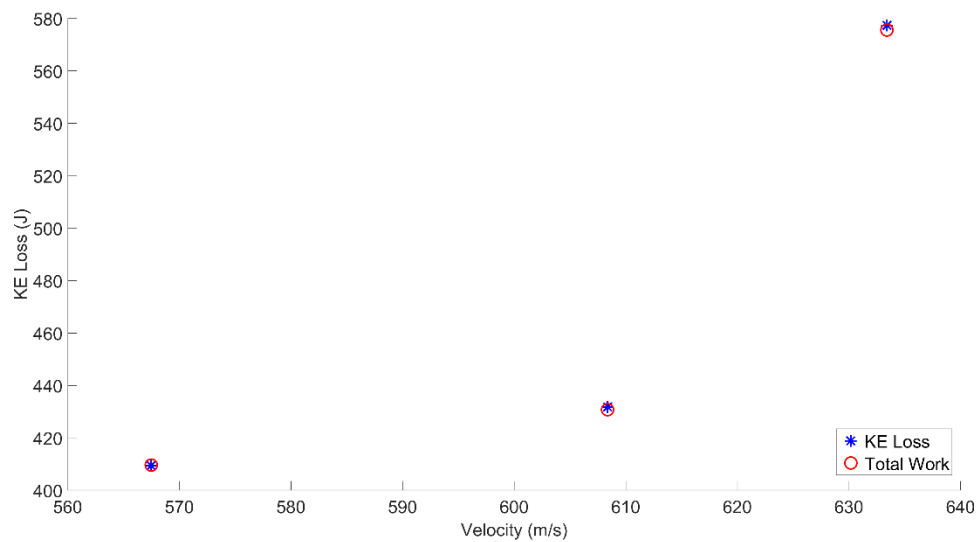


Figure 62. Kinetic energy loss vs. velocity for 0.952 cm AD995 spheres no encapsulation.

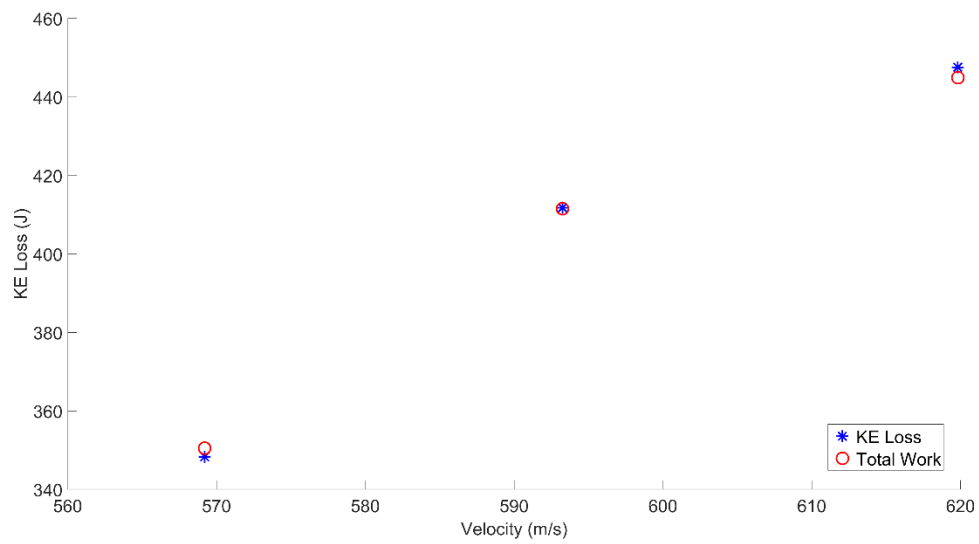


Figure 63. Kinetic energy loss vs. velocity for 0.635 cm AD90 spheres encapsulated in P1000.

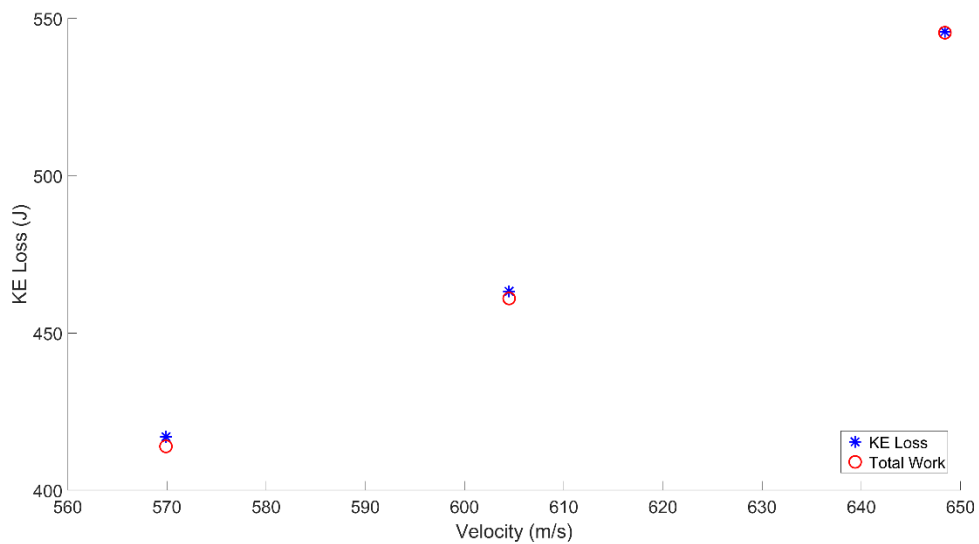


Figure 64. Kinetic energy loss vs. velocity for 0.952 cm AD90 spheres encapsulated in P1000.

Figure 65 and Table 9 present the kinetic energy lost by the 0.30 caliber M2AP projectile for each sample. The SiC tile performed the most work out of all the samples, but the AD90 tile was close in performance. The 0.635 cm AD90 spheres with and without encapsulation performed the worst. The 0.635 cm AD995 (no encapsulation), 0.952 AD90 and AD995 (both with and without encapsulation) performed similarly.

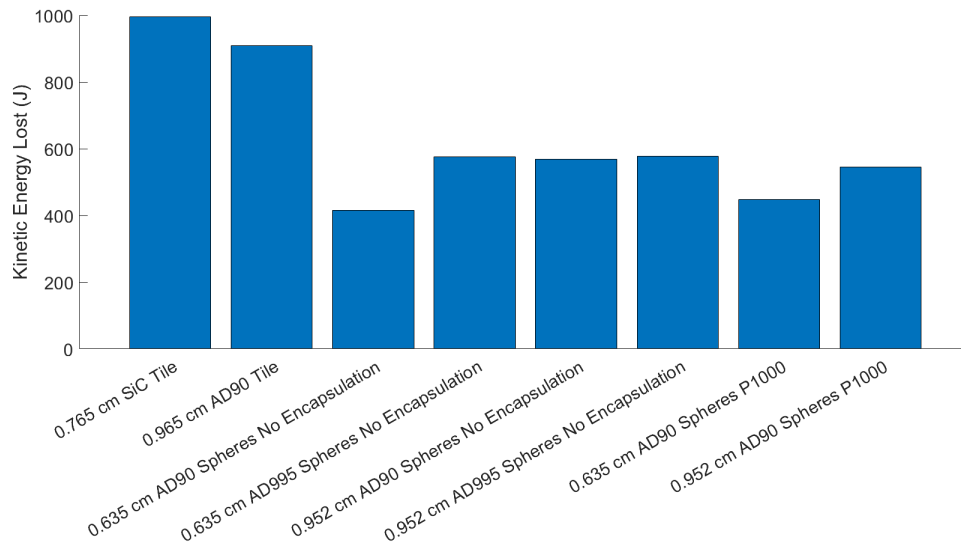


Figure 65. Kinetic energy loss for all eight sample targets at breech pressure 5000 psi.

Table 9. Calculated kinetic energy loss for all eight sample targets at breech pressure 5000 psi.

Sample Front Face Armor System Target	Calculated Kinetic Energy Loss (5000 psi)
0.765 cm SiC Tile	995 J
0.965 cm AD90 Tile	909 J
0.635 cm AD90 Spheres, no encapsulation	415 J
0.635 cm AD995 Spheres, no encapsulation	575 J
0.952 cm AD90 Spheres, no encapsulation	568 J
0.952 cm AD995 Spheres, no encapsulation	576 J
0.635 cm AD90 Spheres, P1000 encapsulation	448 J
0.952 cm AD90 Spheres, P1000 encapsulation	546 J

Q. MASS EFFICIENCY

Mass efficiency is how efficient the samples are at stopping the projectile per their areal density. The equation for mass efficiency was given in Chapter III as equation (3). The energy loss is divided by the areal density. Areal density was listed for each target in Table 5. This normalizes the data to compare how well they perform as a function of areal density. In overall performance, SiC and AD90 tiles outperform the alumina spheres, but regarding mass efficiency (Figure 66 and Table 10) the sphere targets outperform the tiles. The 0.635 cm sphere targets demonstrated the highest mass efficiency. The 0.635 cm AD90 sphere without encapsulation sample target was almost double the SiC tile and even greater as compared to the AD90 tile.

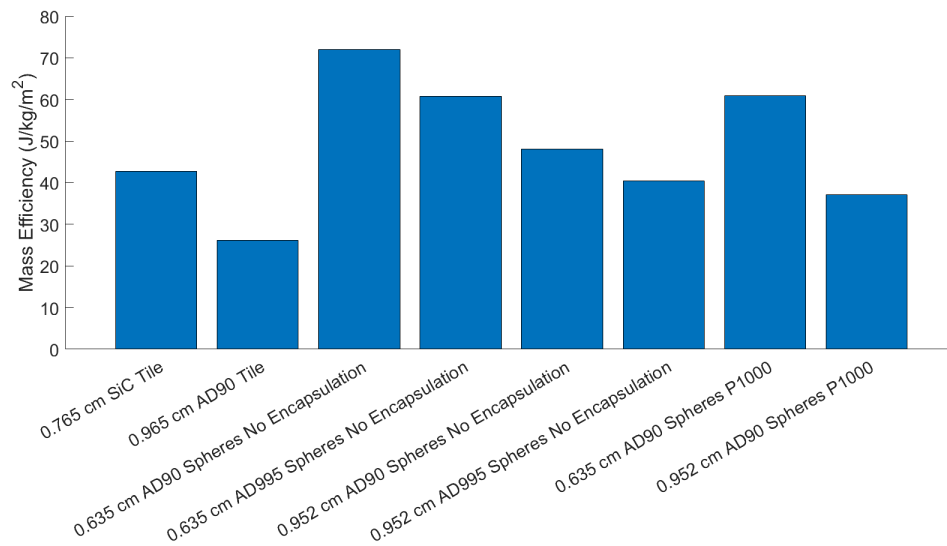


Figure 66. Mass efficiency for all eight sample targets.

Table 10. Calculated mass efficiency for all eight sample targets.

Sample Front Face Armor System Target	Calculated Mass Efficiency (5000 psi)
0.765 cm SiC Tile	42.8 $J/kg/m^2$
0.965 cm AD90 Tile	26.2 $J/kg/m^2$
0.635 cm AD90 Spheres, no encapsulation	72.0 $J/kg/m^2$
0.635 cm AD995 Spheres, no encapsulation	60.7 $J/kg/m^2$
0.952 cm AD90 Spheres, no encapsulation	48.0 $J/kg/m^2$
0.952 cm AD995 Spheres, no encapsulation	40.5 $J/kg/m^2$
0.635 cm AD90 Spheres, P1000 encapsulation	61.0 $J/kg/m^2$
0.952 cm AD90 Spheres, P1000 encapsulation	37.1 $J/kg/m^2$

THIS PAGE INTENTIONALLY LEFT BLANK

VI. CONCLUSION

This thesis studied how different front face armor ceramics (variations in chemistry and geometry) performed against an incident 0.30 caliber M2AP projectile. Performance was measured by both the loss of kinetic energy and calculated work performed against the incident projectile. This technique enabled the ability to capture the force interaction between the projectile and selected front face ceramic armor systems.

In this study eight different front face armor systems were studied against a 0.30 caliber M2AP projectile at three different incident velocities (~630, 610, and 570 m/s). Through the use of a high-speed video camera (5 Mfps), temporal changes in position of the rear of the incident projectile was tracked. Combining the high-speed video with a motion tracking software (TEMA) enabled successful analysis of the kinematic changes of the incident projectile during impact with the selected targets. Temporal resolution of 200 nanosecond (ns) enabled calculations of position, velocity, and acceleration as a function of time. The measured kinematic data allowed for the extrapolation of changes in kinetic energy and work at a 200 ns interval.

Velocity measurements started with a plateau of incident velocity prior to impact, a drop in velocity during impact, then a settling plateau after impact. The velocity data enabled the calculation of kinetic energy loss of the projectile. Measured instantaneous acceleration and change in position along with the known mass of the projectile allowed for the calculation of work of the target system. Through comparisons of kinetic energy loss and/or total work performed, temporal loading behavior was determined.

Observing the instantaneous work and kinetic energy provided insight into when and how much work was being performed by the target systems. The rarefaction wave motion was reflected in the form of interval peaks in the data. Knowing how and when the rarefaction wave affects the ceramic enabled a better understanding of what is occurring during impact.

The performance of the temporal loading behavior of all eight targets was determined using the results from both the calculated kinetic energy loss and total work

performed. The SiC tile and AD90 tile outperformed all variations of alumina sphere targets (995 J for SiC tile and 906 J for AD90 tile at ~ 630 m/s) as displayed in Figure 65 and Table 9. The following conclusions can be made from the energy loss calculations (either kinetic energy loss or total work performed): the tiles performed better than the alumina spheres, alumina of 99.5% purity (AD995) performed better than alumina of 90% purity (AD90), the 0.952 cm diameter of alumina spheres outperformed the 0.635 cm alumina spheres, and encapsulating the alumina spheres in Versalink P1000 hindered performance.

The mass efficiency of each of the sample front face armor system targets was calculated as a function of areal density of the material and calculated energy loss. The 0.635 cm AD90 spheres with no encapsulation performed the best (72 J/kg/m^2), as displayed in Figure 66 and Table 10. The following conclusions can be made from the calculations:

1. The mass efficiency of alumina sphere targets outperformed the tile sample targets.
2. Alumina of 90% purity (AD90) performed better than alumina of 99.5% purity (AD995) based on mass efficiency.
3. The mass efficiency of 0.635 cm diameter of alumina spheres outperformed the 0.952 cm alumina spheres
4. Encapsulation of the alumina spheres in Versalink P1000 hindered performance and reduced the mass efficiency.

Concurrently a study is being performed to understand the loading behavior on the ceramic backed with UHMWPE by LT Brent Morisson. That work analyzes the response of the textile armor backing system to the different front face armor targets.

Additional studies beyond LT Morrison's thesis will be required to understand the handover pressure observed as a function of the initial blunting to the projectile by the front face armor panels. This study would require a soft catch system to enable analysis of the post impact projectile to determine the pressures on the textile armor backing system.

LIST OF REFERENCES

- [1] J. P. Morley, "Effects of ballistic impact on spherical ceramics," M.S. thesis, Dept. of Applied Physics, NPS, Monterey, CA, USA, 2018. [Online]. Available: <https://apps.dtic.mil/sti/citations/AD1060020>
- [2] J. M. Robinson, "Performance of encapsulated ceramic spheres compared to monolithic ceramic plate," M.S. thesis, Dept. of Applied Physics, NPS, Monterey, CA, USA, 2019.
- [3] M. Wilkins, C. Honodel, and D. Sawle, "An approach to the study of light armor," LLNL, Livermore, CA, USA, Rep. UCRL 50284, 1967.
- [4] M. L. Wilkins, "Second progress report of light armor program," LLNL, Livermore, CA, USA, Rep. UCRL 50349, 1967.
- [5] M. L. Wilkins, "Third progress report of light armor program," LLNL, Livermore, CA, USA, Rep. UCRL 50460, 1968.
- [6] M. L. Wilkins, C. F. Cline, and C. A. Honodel, "Fourth progress report of light armor program," LLNL, Livermore, CA, USA, Rep. UCRL 50694, 1969. doi: 10.2172/4173151.
- [7] "Interceptor body armor," *Global Security Organization*. <https://www.globalsecurity.org/military/systems/ground/interceptor.htm> (accessed Oct. 20, 2021).
- [8] Inspector General, DOD, "Army's Management of the Operations and Support Phase of the Acquisition Process for Body Armor," United States Department of Defense, Washington, DC, USA, D-2010-027, Dec. 2009.
- [9] I. G. Crouch, G. V. Franks, C. Tallon, S. Thomas, and M. Naebe, *The Science of Armour Materials*. Elsevier Ltd, 2017.
- [10] National Institute of Justice, "Ballistic Resistance of Body Armor," U.S. Department of Justice, Washington, D.C., USA, Rep. NIJ Standard 0101.06, Jul. 2008.
- [11] "The Next Revision of the NIJ Performance Standard for Ballistic Resistance of Body Armor, NIJ Standard 0101.07: Changes to Test Methods and Test Threats," *National Institute of Justice*. <https://nij.ojp.gov/topics/articles/next-revision-nij-performance-standard-ballistic-resistance-body-armor-nij-standard> (accessed Oct. 19, 2021).
- [12] Inspector General, DOD, "DOD Testing Requirements for Body Armor," United States Department of Defense, Washington, D.C., USA, D-2009-047, Jan. 2009.

- [13] Director, Operational Test and Evaluation, “Standardization of Hard Body Armor Testing,” Office of the Secretary of Defense, Washington, D.C., USA, Memorandum, Apr. 2010.
- [14] I. G. Crouch, “Body armour – new materials, new systems,” *Def. Technol.*, vol. 15, no. 3, Jun. 2019, doi: 10.1016/j.dt.2019.02.002.
- [15] Program Executive Office Soldier, “Interceptor Body Armor (IBA),” U.S. Army, Jan. 2006.
- [16] Toyobo, “PBO Fiber Zylon,” Toyobo Co. LTD, Kita-Ku, Osaka, Japan, 2005.
- [17] W. A. Gooch Jr, “An Overview of Ceramic Armor Applications,” U.S. Army Research Laboratory, Trenčín, Slovakia, IDEE 6th Technical Conference, May 2004.
- [18] J. Kaneshiro, “Picatinny scientists test body armor integrity, protect Soldiers’ lives,” *U.S. Army*, Jan. 18, 2013.
https://www.army.mil/article/94448/picatinny_scientists_test_body_armor_integrity_protect_soldiers_lives (accessed Oct. 22, 2021).
- [19] “New Armor Inspection System ensures ballistic plates safe for deploying Soldiers,” *www.army.mil*.
https://www.army.mil/article/110441/new_armor_inspection_system_ensures_ballistic_plates_safe_for_deploying_soldiers (accessed Oct. 22, 2021).
- [20] W. G. Schulz, “What’s that stuff? Body armor,” *Chemical & Engineering News*, Mar. 29, 2019. <https://cen.acs.org/articles/88/i13/Body-Armor.html> (accessed Oct. 22, 2021).
- [21] “CoorsTek AD-90 Alumina (nom. 90% Al₂O₃).”
<http://www.matweb.com/search/DataSheet.aspx?MatGUID=0e9742efe285442fb5a63b46daee2a41> (accessed Oct. 19, 2021).
- [22] MatWeb, “CoorsTek RB B4C reaction-bonded boron carbide,” *MatWeb LLC*, 2021 1996.
<http://www.matweb.com/search/DataSheet.aspx?MatGUID=91dde6c8105f4ea7af89d6fd428bb4cf> (accessed Oct. 19, 2021).
- [23] Saint-Gobain, “Hexoloy SP SiC material,” *Saint-Gobain Performance of Ceramics & Refractories*, 2021. <https://www.ceramicsrefractories.saint-gobain.com/materials/silicon-carbide-sic/hexoloy-silicon-carbide-material/hexoloy-sp-sic-material> (accessed Oct. 19, 2021).

- [24] MatWeb, “CoorsTek AD-995 alumina (nom. 99.5% Al_2O_3),” *MatWeb LLC*, 2021 1996.
<http://www.matweb.com/search/DataSheet.aspx?MatGUID=ab23341b30ed480fa4372524eb49e465> (accessed Oct. 26, 2021).
- [25] Bayville Chemical Supply Company Inc, “Versalink P-1000,” Deer Park, New York, USA.

THIS PAGE INTENTIONALLY LEFT BLANK

INITIAL DISTRIBUTION LIST

1. Defense Technical Information Center
Ft. Belvoir, Virginia
2. Dudley Knox Library
Naval Postgraduate School
Monterey, California